

**MEM 493
SENIOR DESIGN**



P15 - SWERVE ROBOTIC PLATFORM

Harrison Katz (hzk27@drexel.edu)
Alexander Nhan (an497@drexel.edu)
Frederick Wachter (faw28@drexel.edu)
Matthew Wiese (mcw327@drexel.edu)

Submission Date

14 May 2018

Head Advisor

Dr. Ajmal Yousuff

Co-Advisor

Dr. Tein-Min Tan

Sponsors

Joshua Geating, SICK Sensors, Botstiber Senior Design Competition,
ASME Philadelphia, Drexel MEM Department

Abstract

The Swerve Robotic Platform is a three-wheeled, autonomy-enabled vehicle that is capable of carrying large loads while moving at high accelerations. This platform is targeted for the entertainment, warehouse optimization, and personal mobility industries. This platform was designed, fabricated, and tested using modern tools including motion capture systems, advanced machining techniques, computer simulations and software, as well as state-of-the-art sensors. The vehicle was designed and manufactured to be lightweight and robust by using finite element analysis, iterative design processes, and computer controlled tooling. The platform software was developed in the ROS framework and utilized the Gazebo physics simulator in order to generate data sets and test autonomy algorithms in both simulation and on the existing platform. System models, sensors, as well as sensing techniques were used to provide the platform with the ability to understand its local environment and its location within that environment. A human-machine interface is provided with the platform to allow for intuitive control of the system. The platform adheres to ASTM, AWS, and AISC standards pertaining to system design, analysis, and testing.

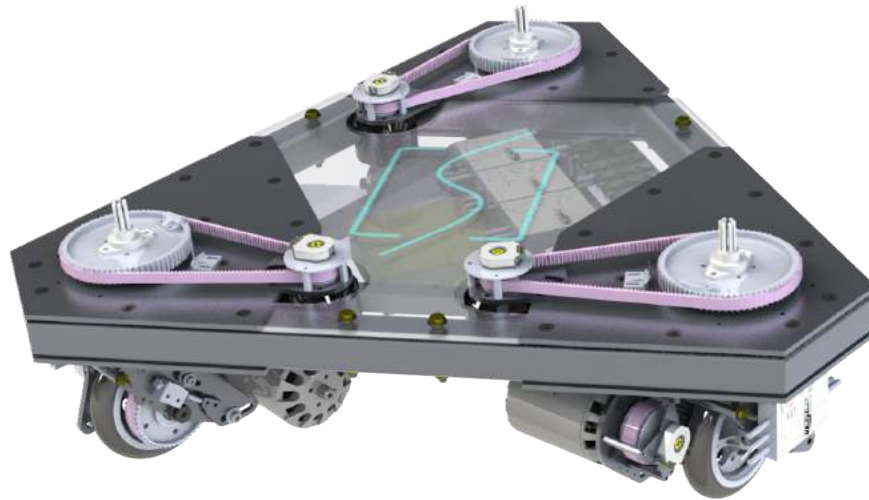


Table of Contents

Abstract	2
Table of Contents	3
List of Figures	9
List of Tables	10
Terminology	12
Introduction	12
Project Overview	12
Use Cases and Required Movements	13
Standards, Referenced Publications, and Practices	13
Market Need	13
Final Design Package	14
Mechanical Design	14
Chassis Assembly	15
Wheel Assembly	16
Structural and Mechanical Analysis	17
Analysis Overview	18
Structural Analysis	18
Mechanical Analysis	24
Manufacturing Process	28
Critical Path to Manufacturing Success	29
Gusset Plates	29
Chassis Hollow Structural Tubes	31
Shafts	32
Side Plates	33
Connecting Block	34
Wheels	36
Pulleys	36
Electronics	39
Electronics Selection Overview	39
Computing Hardware	39
Actuators	40
Sensing	40
Calibration Block	40
Motor Control	41
Safety Features	41
Electronics Layout	41
Software	41
Software Architecture Overview	41
Software Development Tool Utilization	42
Robot Frame Definitions	43
Simulation Environment	44
Communication Protocols	44
Software Version Control	45
Algorithms and Autonomy	45
Kinematic and Dynamic Modeling	46
Laser Scan Matching	48
Occupancy Grid Mapping	48

Particle Filtering	50
Path Planning	52
Robot Test Platform	53
Testing and Validation	54
Welded Material Strength Verification	54
Software Architecture Validation	56
Communication Validation	57
Visual Qualitative Validation Tools	58
Autonomy Algorithm Validation and Dataset Generation	59
Vehicle Weight Validation	60
Future Work	60
Finite Element Model Validation	60
Speed and Acceleration Testing	61
Agility Testing	62
Closing Remarks	62
References	63
Acknowledgements	64
Appendix	65
Design and Analysis Process	65
Mechanical Design Process	66
Structural and Mechanical Analysis Process	67
Protocol Comparison for Communicating with VESC's	69
Further Optimization with Path Planning	69
Electronics Safety Features Additional Information	70
Project Management	70
Personnel	70
Organizational Tools	70
Software Usage	70
Project Schedule	71
Review Processes	71
Project Budget	71

List of Figures

- Figure 1.** Existing Solutions from Research and Industry [3] [4] [5].
- Figure 2.** Overview of the Chassis Design.
- Figure 3.** Cross Sectional View of the Chassis Crush Tubes.
- Figure 4.** Overview of the Wheel Assembly Design.
- Figure 5.** Cross Sectional View of the Wheel Assembly Installed in Chassis.
- Figure 6.** Visual Representation of Load Cases Used in Finite Element Model.
- Figure 7.** Finite Element Models of the Chassis Assembly (Left) and Wheel Assembly (Right).
- Figure 8.** Finite Element Assembly of the Vehicle Used for Analysis.
- Figure 9.** Von Misses Stress Contour Plot of Expected Stress (30deg Load Case).
- Figure 10.** Absolute Principal Stress Contour Plot of Expected Stress (60deg Load Case).
- Figure 11.** Von Misses Stress Contour Plot of Expected Stress (Perpendicular Load Case).
- Figure 12.** View of Drive Pulley (Left) and Diagrams of Pulley-Wheel Interfaces.
- Figure 13.** Geometric Diagram (Left), Assembly View (Center), Cross Sectional View (Right).
- Figure 14.** Geometric and Force Diagram (Left) and Assembly View (Right).
- Figure 15.** Completed Critical Path to Success for Manufacturing.
- Figure 16.** View of Waterjet Cutting Gusset Plates (Left), Plates Post Waterjet Cutting (Right).
- Figure 17.** Finding Hole Center (Left), Boring Size of Hole (Center), Test Fit Hardware (Right).
- Figure 18.** Drawing for Structural Tubes (Left), Drilling Holes for Crush Tubes (Center,Right).
- Figure 19.** Crush Tube Pre Welding (Left), Post Welding (Center), Assembled (Right).
- Figure 20.** Machining Outside Shaft Dimension (Left), Inside Dimension of Shaft (Center, Left).
- Figure 21.** Locating Center of Shaft (Left), Starting Holes (Center), Tap Drilling (Right).
- Figure 22.** Tapping 10-32 Threading into Shaft (Left), Completed Shaft (Right).
- Figure 23.** Load Path of Wheel Assembly Mechanism.
- Figure 24.** Side Plate Fixture (Left), Side Plate Interface (Center), Final Product (Right).
- Figure 25.** CAM simulation (Left), Actual CNC Machining (Center), Finished Part (Right).
- Figure 26.** Mounting Block (Left), Locating (Left Center), Drilling (Right Center), Tapping (Right).
- Figure 27.** Test Assembly to Verify Tolerancing (Left), Side Plate, Block, Shaft Assembly (Right).
- Figure 28.** Locating (Left), Bolt Pattern (Left Center), Nut Mod (Right Center), Assembly (Right).
- Figure 29.** Enlarging Dia (Left/Left Center), Adding Lip (Right Center),Mount to Mill (Right).
- Figure 30.** Remove Hub (Left), Locate (Left Center), Pattern (Right Center), Assembly (Right).
- Figure 31.** Enlarged (Left), Pocket (Left Center), Mill Mount (Right Center), Removal (Right).
- Figure 32.** Locating Center (Left), Drilling Hole Pattern (Center), Fully Assembled (Right).
- Figure 33.** Broach Collar (Left), Broach Setup with Press (Center), Close up of Broach (Right).
- Figure 34.** Pulley and Keyway Broach (Left), Motor and Key (Center), Fit Keyed Pulley (Right).
- Figure 35.** Calibration Block Diagram.
- Figure 36.** Simplified Electronics Layout.
- Figure 37.** Software Architecture Visual Depiction.
- Figure 38.** Frame Definition of the Platform.
- Figure 39.** Visual Representation of Platform Frames Using Simplified Geometry.
- Figure 40.** Simplified Platform Simulated in Gazebo (left) and displaying data from ROS (right).
- Figure 41.** Protocol for UART Communication with VESC using an 8 bit payload.
- Figure 42.** Protocol for UART Communication with VESC using a 16 bit payload.
- Figure 43.** Protocol for CAN Communication with VESC.
- Figure 44.** Diagram of Variables for the Kinematic Model.
- Figure 45.** Force Diagram of Wheel Assembly and Resulting Force Calculations.
- Figure 46.** Occupancy Grid Mapping Computations and Visual Depiction.
- Figure 47.** Occupancy Grid Map Built Using Exact Pose and Clean LiDAR Data.
- Figure 48.** Occupancy Grid Map Using Pose Estimates and Noisy Data.

Figure 49. Depiction of State Update Using Particle Filter.

Figure 50. Using Particle Filter to Estimate State Over Time on an Occupancy Grid.

Figure 51. Valid Path Generated Using A* Algorithm and a Known Map (Obstacles in Red).

Figure 52. THOR Robot Test Platform with LiDAR Mounted.

Figure 53. Loading Configuration and Equations for a 4-Point Bend Test.

Figure 54. Data Collection Devices for Test - Isometric View (Left) and Side View (Right).

Figure 55. Resulting DIC Data from the Four-Point Bend Test.

Figure 56. Validating Software Architecture Using Gazebo (LiDAR ray visualized in blue).

Figure 57. Teleoperating the Robot Test Platform on Drexel University Wifi Network.

Figure 58. MATLAB GUI to Visually Validate Platform Kinematics.

Figure 59. Teleoperating the Robot Test Platform in a Motion Capture Room with Obstacles.

Figure 60. Occupancy Grid Generated from Dynamic Dataset 3.

Figure 61. Max Principal Stress Contour Plot of Chassis Under 300lbs.

Figure 62. Position, Velocity, and Acceleration Curves of Usain Bolt Across 100 Meters.

Figure 63. Designated Course Setup to Verify Needs 1 and 2.

Figure A1. Mechanical iterations of swerve drive assembly.

Figure A2. Stress Concentration Factors for Tension Plates with Holes Near Edges [A2].

Figure A3. Quadratic Fit Given AISC Bolt Preload Values and Interpolated Preloads.

Figure A4. Countersink Bolt Force Diagrams and Resulting Calculations.

Figure A5. Images of Team Personnel.

Figure A6. Finalized Project Schedule.

List of Tables

- Table 1.** List of Standards and Specifications Used for Developing Swerve.
- Table 2.** Mechanical Properties for Typical Materials Used in Analysis [6] [7]
- Table 3.** Safety Margins in the Aluminum Specification (Table 6.1) [7]
- Table 4.** Safety Factor Summary by Load Case - Structural
- Table 5.** RCSC Bolt Calculations for 1/4-20 Bolts.
- Table 6.** RCSC Bolt Calculations for 1/4-20 Bolts (Continued).
- Table 7.** Safety Factor Summary by Load Case - Mechanical.
- Table 8.** Bearing Calculations and Resulting Force Margins.
- Table 9.** Timing Belt Pulley Calculations and Resulting Force Margins.
- Table 10.** Drive Wheel Shaft Calculations and Resulting Stress Margins.
- Table 11.** Motor Bolts Calculations and Resulting Stress Margins.
- Table 12.** Project Needs and Target Specifications.
- Table 13.** VICON Motion Capture Dataset Information.
- Table A1.** List of Review Processes.
- Table A2.** High Level Project Costs.
- Table A3.** Total Project Funding.

Terminology

Swerve Robotic Platform	The Fabricated Vehicle
Hollow Structural Section (HSS)	Hollow Tubes for Fabrication
DIC Camera	Digital Image Correlation Camera
LIDAR Sensor	Light Detection and Ranging
VICON	External Motion Capture Systems
ROS	Robot Operating Systems
BLDC	Brushless Direct Current Motor
VESC	BLDC Motor Controller (Vedder Electronic Speed Controller)
TCP	Transmission Control Protocol
UART	Universal Asynchronous Receiver-Transmitter
CAN	Controller Area Network
SBC	Single Board Computer
SICK	Advanced Sensors Company
Platform	Swerve Robotic Platform
Environment	Surrounding of the platform (static/dynamic)
Patron	Human Operator
UNIX	Type of Operating System
FEA/FEM	Finite Element Analysis / Finite Element Modeling
ASME	American Society of Mechanical Engineering
THOR	Three Omni-Wheeled Platform (Test Platform)
Yaw Components (Pulley, Motor)	Components that Orient the Wheels
Propulsion Components (Pulley, Motor)	Components that Drive the Wheels
COTS Parts	Consumer off the Shelf Parts
CAD/CAM	Computer Aided Drawing/Computer Aided Manufacturing
Wheel Assembly	Mechanisms Below the Chassis
GUI	Graphical Human Interface
Slack, Google Drive, GitHub	Team Communication/File Sharing/ Software Hosting

Introduction

Project Overview

The stakeholder would like to have a robotic platform that is able to support payloads up to a 95th percentile male (300 lbs) and is able to move at speeds and accelerations faster than Usain Bolt. Additionally, this platform must have omni-directional and variable speed capabilities controlled by a human operator through a human-machine interface provided with the platform. This platform must also be able to be disassembled and reassembled within a reasonable time.

Use Cases and Required Movements

The Swerve Robotic Platform is designed and engineered to be a three-wheeled, omnidirectional, autonomy-enabled mobile platform. The vehicle is intended to be as lightweight and as nimble as possible by incorporating holonomic movements and high-torque, high-velocity brushless DC motors. Each of the three wheels is capable of independent yaw and propulsion. Additionally the vehicle is designed and analyzed to carry payloads up to 300lbs without appreciable damage, and it is capable of traveling at speeds exceeding 28 miles per hour and accelerations up to 32.2 ft/s^2 (1G).

Standards, Referenced Publications, and Practices

Table 1 below lists the standards and practices that were referenced and implemented while developing the Swerve platform. The referenced standards and specifications are developed by various organizations and publications, influence multiple industries, and affect the design and analysis of every aspect of the Swerve platform.

Table 1. List of Standards and Specifications Used for Developing Swerve.

ASTM F2291-17: *Standard Practice for Design of Amusement Rides and Devices*

ASTM E855-08: *Bend Testing of Metallic Flat Materials for Spring Applications*

RCSC - 2009: *Specification for Structural Joints Using High-Strength Bolts*

ASIC 360-16: *Specification for Structural Steel Buildings*

AWS D1.2: *Structural Welding Code - Aluminum*

Google C++ Style Guide: *Programming Style Guidelines*

ROS C++ Style Guide: *Programming Style Guidelines*

Doxygen: *Auto Code Documentation*

ASTM F2291-17 was referenced for applicable impact and dynamic factors related to the entertainment industry [1]. ASTM E855-08 was referenced for test procedures related to metallic material failure. RCSC-2009 was used for bolted connection calculations and preload values. ASIC 360-16 was referenced for safety factors related to steel connections [2]. AWS D1.2 was used for welded aluminum specifications and standards. Google C++ and ROS C++ style guides were adhered to for programming and code creation. Finally, Doxygen was referenced and adhered to for auto code documentation.

Market Need

Swerve drive is the ability to control both full 360 degree directional orientation and rotational velocity of a wheel. This concept is not new but there are only a small amount of commercially available products that incorporates such a drive system. Swerve drive allows for a highly nimble robot that can accelerate in any direction from any orientation. The unique drive mechanism also enables complex movements such as coupled translation and rotation. Currently, few industries have implemented the swerve drive train.

A popular market for swerve drive includes student design competition, such as the First Robotics Competition, in which teams benefit from having highly nimble and agile robots that can out maneuver the non-holonomic drive systems of competitors. These types of machines are designed for speeds about 15 mph and can weigh up to 100 pounds depending on competition rules. The First Robotics Competition does not allow the use of brushless direct current (DC) motors, thus only brushed DC motors have been implemented, which generally have smaller torque and lower power to weight ratio than brushless DC motors. An example of these types of swerve drive competition robots can be seen in leftmost image of **Figure 1**.

Another existing solution is from NASA who built a large 2,000 pound swerve drive vehicle that can achieve a max speed of 40 miles per hour and a payload of about 500 pounds. This research project relies on restricted swerve drive mechanisms in which the wheels can only be directionally controlled up to 180 degrees, instead of continuous 360 degree rotation. This can be seen below in the center image of **Figure 1**.

Finally, an existing solution within the potential market related to automated material transport is a robot from Fetch Robotics seen below in the rightmost image of **Figure 1**. This robot has a maximum speed of 3.3 miles per hour, can carry a total payload of 177 pounds, and features a non-holonomic drive system than cannot make the nimble movements that a swerve drive system can achieve. A nimble robot of this scale and power has a large array of potential market and private industrial impacts including the warehouse optimization, entertainment, and personal transportation industries.



Figure 1. Existing Solutions from Research and Industry [3] [4] [5].

Final Design Package

Mechanical Design

The vehicle is a product of two main subassemblies including a chassis structure and three identical wheel assemblies. Each of the wheel assemblies is connected to the chassis through the center holes in the gusset plates, equidistant from the chassis geometric center shown in **Figure 2**. The radial symmetry allows for general, unbiased movement of the platform in all directions as well as an optimized wheelbase for various payloads. To allow the platform to remain disassemblable there were no gross, permanent fastening methods used. Although a radial symmetry exists within the system, a front was determined to define the vehicle orientation and the direction the patron would face during normal operation. Yaw motors are mounted to the top of the chassis assembly, and drive motors are mounted below each wheel assembly. In order to decouple the yaw and drive motion, slip rings were used to transfer power and data to the drive motors while still allowing 360deg continuous yaw rotation.

Chassis Assembly

The chassis was assembled using hollow structural sections (HSS) bolted together through gusset plates on the top and bottom surfaces of the assembly. The front gusset plates slightly differ from the rear in that there is no additional standing room for a patron. A plane frame design was chosen for the chassis for the increased strength and ease of manufacturing. Additionally, crush tubes were welded into multiple, local locations within the beams to prevent section warping and residual stresses when applying bolt preload. In order to keep a generic platform, flathead bolts were chosen to assemble the chassis so the top surface remains flush. The chassis is secured with nylon lock nuts on the bottom surface to remain secure within the potentially vibratory environment.

The HSS members are 1.5" sq. sections with radiused corners to eliminate any stress concentrations and each gusset plate is 0.18" thick. The entire chassis is about 1.88" tall from the bottom gusset plate to the top gusset plate. Each yaw motor for the front, left, and right wheel assemblies are mounted to the top gusset plates. The motor mount plates pivot around a shoulder bolt and allow for belt tensioning by securing cap screw bolts. A detailed image of the chassis can be seen in **Figure 2**, and a cross section view of the crush tube assembly can be seen in **Figure 3**.

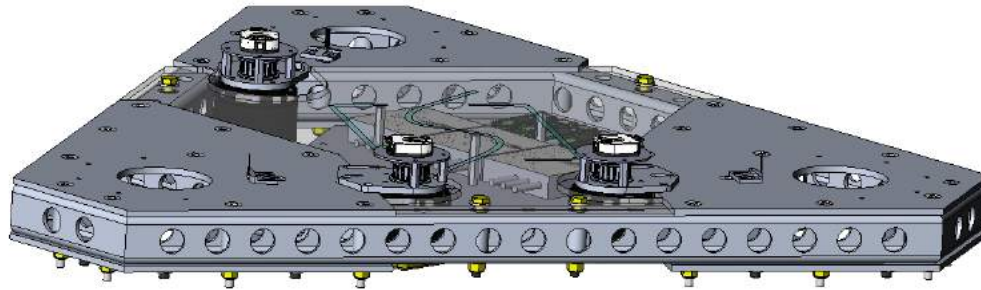


Figure 2. Overview of the Chassis Design.

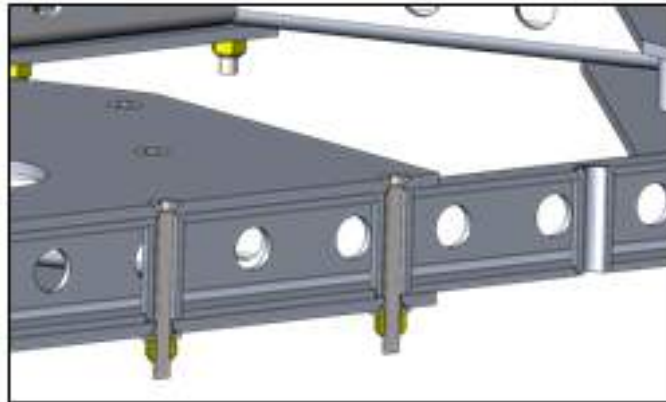


Figure 3. Cross Sectional View of the Chassis Crush Tubes.

Wheel Assembly

Each wheel assembly was installed in the chassis using two radial, flanged bearings, a thrust bearing, and a predetermined stack up of belleville washers and shims which preload both radial bearings to ~50lbs. Both upper and lower radial bearings react the bending moment produced by the torque on the drive wheel, while the thrust bearing and belleville washers react the preload and vertical load. A large diameter, short, hollow shaft was manufactured out of 6061-T6 to provide the largest moment capacity and smallest deflection under loading. This shaft includes tapped holes on the top and bottom that bolt to the yaw belt pulley and connecting block respectively. Additionally, the hollow shaft allows for the slip ring housing and wires to run concentric to the yaw belt pulley.

Vertical side plates were bolted to the tapped holes on the connecting block, and this created the primary structure for the wheel assembly. Both left and right side plates were manufactured identically for ease of manufacture and modularity. Additionally, standoffs that span the wheel well length were fabricated to add rigidity to the structure in order to prevent buckling and bending failure. The drive wheel shaft, created using a 10mm diameter shoulder bolt, was torqued to add preload to the bearing stackup as shown in **Figure 4**. Standoffs of various lengths were manufactured to transfer the preload between each bearing race internal to the drive wheel pulley and drive wheel.

The drive motor mounted to an additional motor plate with a shoulder bolt that allowed the motor to rotate similar to the yaw motor mounts. The drive motor was properly positioned using a tensioning bolt and jam nut combination to provide fine tuning. A threaded block was bolted to the side plate and the shank of the bolt was then forced against the motor mount so that it rotated around the shoulder bolt. Once a proper motor orientation was chosen, the additional bolts were tightened to react the motor torque and self-weight. The tensioning bolt remained engaged as a redundancy if the other bolts lost preload and slipped. Additionally, the motor controllers were mounted on the mirrored side of each wheel assembly. The cross section of the wheel assembly is shown below in **Figure 5**.

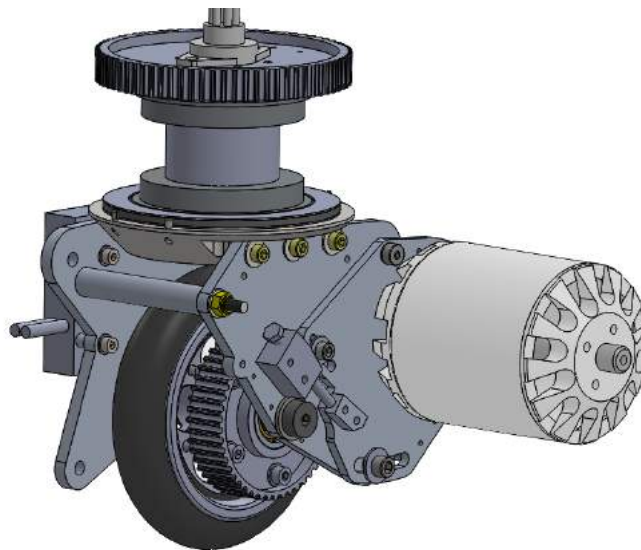


Figure 4. Overview of the Wheel Assembly Design.

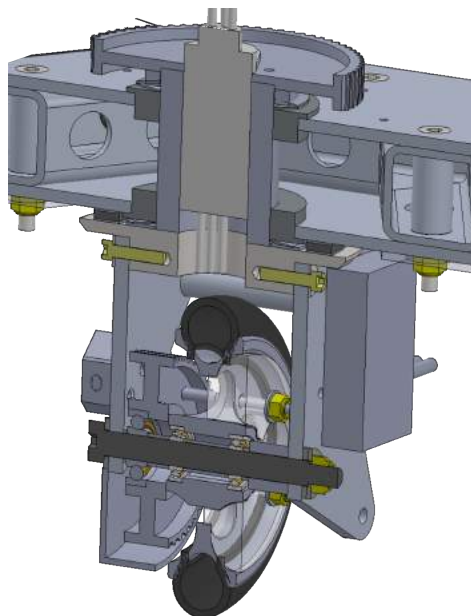


Figure 5. Cross Sectional View of the Wheel Assembly Installed in Chassis.

Structural and Mechanical Analysis

Analysis Overview

The vehicle is intended to accelerate and maneuver as quickly as possible. For design and analysis purposes, the acceleration rate was chosen to be 32.2 ft/s^2 (1g). Additionally, the vehicle is intended to carry a single passenger who stands on top of the vehicle in specifically marked locations. To accommodate different people, a large patron weight of 300lbs was assumed for analysis purposes as a worst case. By leaning in a desired direction, the vehicle will accelerate in that direction, similar to a segway. Using pressure sensors, the vehicle accelerates at a rate that prevents the vehicle and leaning patron from tipping. Using ABAQUS/CAE, a finite element model was created and analyzed per the specifications listed above. Additionally, supporting structural and mechanical calculations were completed to validate the proposed design.

This system is intended to be used for recreation, for short periods of time, and in dry as well as clean environments. Therefore, fatigue considerations and material corrosion are beyond the scope of the analysis. For analysis success, the mechanical and structural components are expected to pass conservative safety factors for strength load cases.

Below are the material properties for the general materials used in the proceeding analysis. Additionally, the required safety factors for aluminum are listed as well. If a different material or safety factor is used for analysis, it will be noted specifically within that section of the report. The welded aluminum allowables are highlighted for clarification in addition to the aluminum safety factors used for the analyses. For simplicity, Building Type structures are static load dominated, while Bridge Type structures are dynamic load dominated.

Table 2. Mechanical Properties for Typical Materials Used in Analysis [6] [7]

Structural Materials	Material Name	Density [lb / in ³]	E -Modulus [psi]	Poisson -	Yield σ [psi]	Ult. σ [psi]
	Aluminum 6061-T6	0.098	9.9E +06	0.33	35000	42000
	Structural Steel A36	0.284	2.9E +07	0.32	36000	55000
	Welded 6061-T6	0.098	9.9E +06	0.33	15000	24000

Table 3. Safety Margins in the Aluminum Specification (Table 6.1) [7]

Type of Structure	Yield Strength	Ultimate Strength
Building Type	1.65	1.95
Bridge Type	1.85	2.20

Structural Analysis

The structural components were analyzed for full-load, full performance operation. During operation, the patron will lean in a desired direction at a specific angle. This places the patron Center of Gravity (CG) away from the vehicle, and a calculated acceleration is required to avoid tipping. A lumped point mass of 300lbs was placed in the finite element model at the specified location to represent the patron CG. The contact locations of the wheels were constrained to only allow rotation (translations fixed) and global accelerations were applied to the model to represent the accelerations of the vehicle. Important factors and values used in the analysis are listed below:

- A Dynamic Factor was not considered since it is included in the required safety factor
- A 1.2 Impact Factor was applied to all accelerations per ASTM F2291-17 [1].
- The Patron CG is located 40.7in on top of the gusset plates per Wiley [8].

To simulate 1g acceleration in any direction, the patron CG and acceleration vectors were manipulated for load cases at 30deg increments from 0deg to 180deg. Since the structure is symmetric about the X-Z plane, only the first 180deg need to be analyzed. Nine load cases were analyzed using ABAQUS/CAE including 7 straight line acceleration load cases (0deg - 180deg) as well as one perpendicular load case where the wheels are oriented 90deg from the direction of travel. This case is to simulate high speed cornering at 1g.

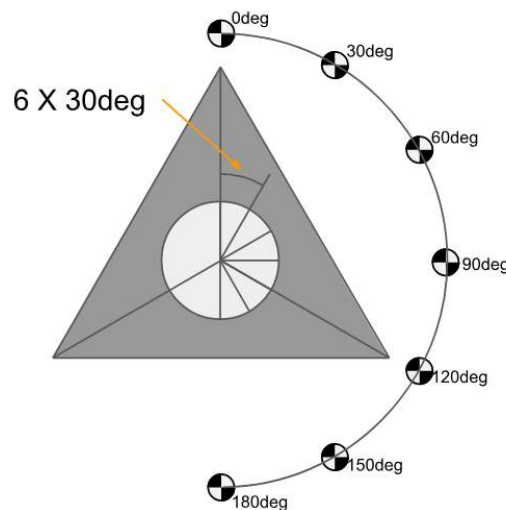


Figure 6. Visual Representation of Load Cases Used in Finite Element Model.

The expected stresses and resulting safety factors for the structural components are listed in **Table 4**. All analyzed components meet the required strength, and the load cases with the smallest margin for each part is highlighted in green.

Table 4. Safety Factor Summary by Load Case - Structural

Load Case	Assem. Criteria	Allow σ [ksi]	Expect σ [ksi]	Expect SF	Required SF
0deg	Chassis Assembly	35.0	14.28	2.45	1.85
	Chassis Welded	24.0	7.14	3.36	2.20
	Wheel Assemblies	35.0	6.32	5.54	1.85
30deg	Chassis Assembly	35.0	14.75	2.37	1.85
	Chassis Welded	24.0	7.81	3.07	2.20
	Wheel Assemblies	35.0	8.77	3.99	1.85
60deg	Chassis Assembly	35.0	8.67	4.04	1.85
	Chassis Welded	24.0	8.63	2.78	2.20
	Wheel Assemblies	35.0	5.66	6.18	1.85
90deg	Chassis Assembly	35.0	6.80	5.15	1.85
	Chassis Welded	24.0	7.78	3.08	2.20
	Wheel Assemblies	35.0	8.31	4.21	1.85
120deg	Chassis Assembly	35.0	10.68	3.28	1.85
	Chassis Welded	24.0	5.43	4.42	2.20
	Wheel Assemblies	35.0	6.70	5.22	1.85
150deg	Chassis Assembly	35.0	12.49	2.80	1.85
	Chassis Welded	24.0	4.26	5.64	2.20
	Wheel Assemblies	35.0	6.35	5.51	1.85
180deg	Chassis Assembly	35.0	10.82	3.24	1.85
	Chassis Welded	24.0	3.61	6.66	2.20
	Wheel Assemblies	35.0	4.82	7.26	1.85
Perpendicular	Chassis Assembly	35.0	7.13	4.91	1.85
	Chassis Welded	24.0	8.53	2.81	2.20
	Wheel Assemblies	35.0	8.61	4.07	1.85

A finite element model was created for the vehicle. The chassis HSS members as well as the crush tubes were idealized as 2D linear shell elements with an element thickness equal to the HSS thickness (0.125in). Similarly, the chassis gusset plates were modeled as 2D linear shell elements with a thickness equal to the plate thickness (0.188in). Finally, the bolts were modeled as 1D circular beam elements with a cross sectional area proportional to twice the bolt diameter. This increase in diameter is to ensure the model is sufficiently stiff and the deflections are restricted to the linear, elastic regime. The patron mass of 300lbs was modeled as a lumped point mass and was moved to various locations in the model depending on the load case. In order to accurately represent a patron foot connection, a distributed Coupling Constraint was used to connect the point mass to specified standing locations on the chassis gusset plates. The Coupling Constraint was chosen to eliminate unequal load distribution, and the connection restricted translation while the rotational deflection components were released.

The wheel assembly was primarily modeled using 2D linear shell elements with the specified element thickness shown below. For the connecting plate, 3D linear tetrahedral elements were used to accurately represent the complex machined part. In order to simplify the model and limit the number of nodes throughout the model, the nodes at the bottom of the steering shaft (shown in yellow below) were merged with the neighboring nodes on the connecting plate. Additionally, a lumped point mass was added to the model to represent the drive motor, and the mass was rigidly connected to the corresponding mounting locations. Finally, a point representing the bottom of the wheel was added to the model, and the point was rigidly connected to the nodes representing the drive axle. An overview of the chassis assembly and wheel assembly finite element models can be seen below.



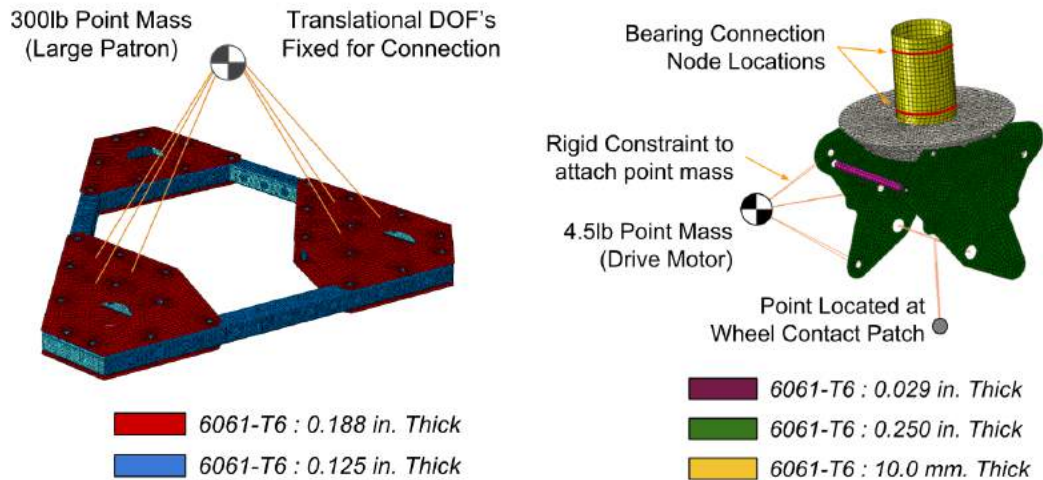


Figure 7. Finite Element Models of the Chassis Assembly (Left) and Wheel Assembly (Right).

The finite element assembly was created with one instance of the chassis model and three instances of the swerve assembly models. The swerve assemblies were placed in the proper positions using datum points created during preprocessing, and the direction angle was varied depending on the load case. To accurately represent a wheel on the ground, the points created on the swerve assembly model level were constrained on the assembly level. The constraint used restricted translations in all directions, but it allowed all rotations to eliminate the potential for the wheel to inaccurately react a moment. Additionally, translation constraints were added between the gusset plates and swerve assemblies to simulate a bearing connection. However, the top bearing connection included a rotational constraint to represent the torque applied from the steering drive motor. Finally, global model accelerations were added per load case to represent the loading from the wheel dynamics. The assembly finite element model can be seen in detail below.

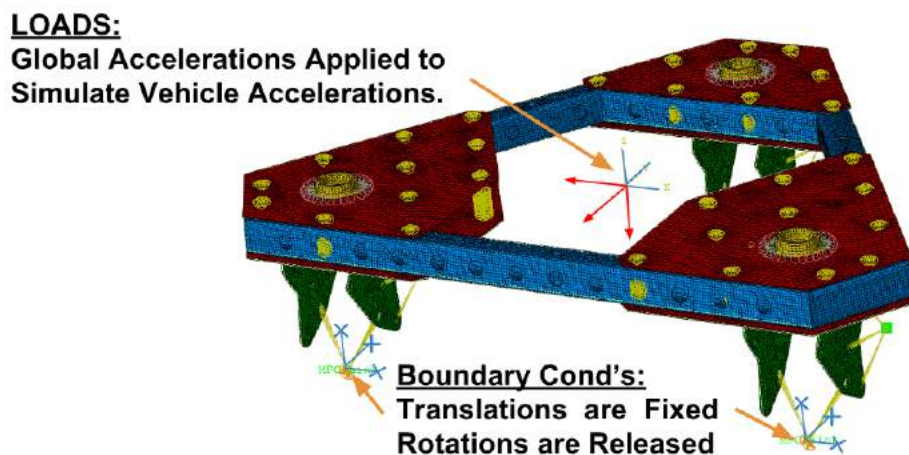


Figure 8. Finite Element Assembly of the Vehicle Used for Analysis.

Stresses evaluated in the chassis gusset plates are compared to the dynamic loading (bridge type) yield strength safety factor of 1.85. Stresses near bolted and patron connections are evaluated two elements away from the connection to ignore singularities and artifacts of the simulation. This provides a nominal stress in the parent material at the connection location. Below is the Von Mises stress contour plot for the load case resulting in the most severe stresses in the gusset plates. The expected stresses are below the allowable stress for the 6061-T6 parent material and result in a passing safety factor of 2.37 compared to the minimum 1.85. The most severe loading condition was determined to be the 30deg Load Case.

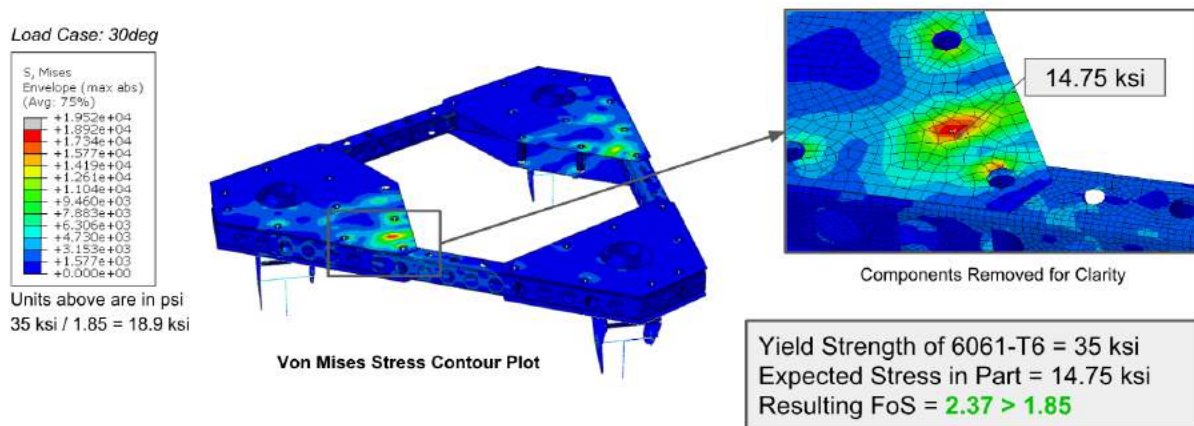


Figure 9. Von Mises Stress Contour Plot of Expected Stress (30deg Load Case).

Stresses evaluated in the chassis beam members are compared to the dynamic loading (bridge type) ultimate strength safety factor of 2.20. Stresses at welded connections are evaluated at the most severe nodal location, typically at the node connecting the crush tube and the chassis beam. Evaluating stresses at this location is to account for welding defects despite the conservative stress values due to the singularity of connecting shell elements at 90deg angles. Below is a Maximum Principal stress contour plot for the load case resulting in the most severe stresses in the welded connections. The expected stresses are below the allowable stress for the weld and result in a passing safety factor of 2.78 compared to the minimum 2.20. The most severe loading condition was determined to be the 60deg Load Case.

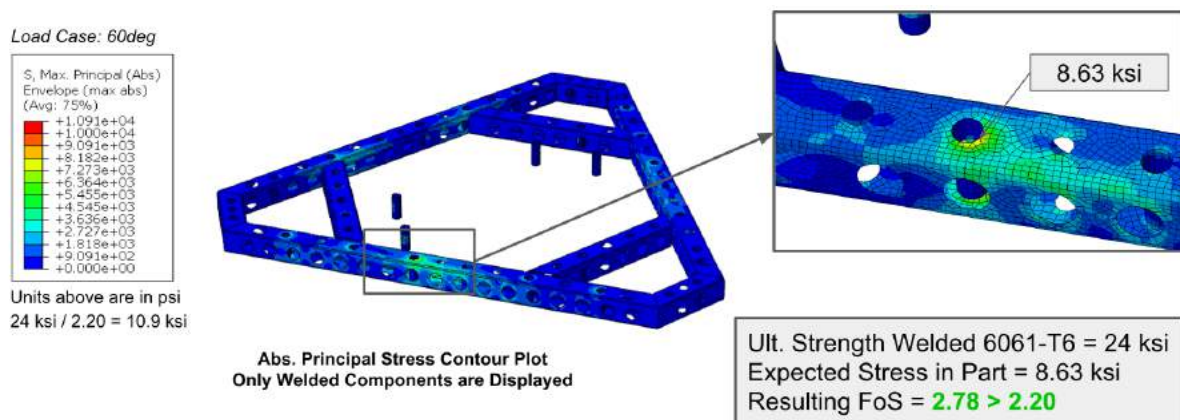


Figure 10. Absolute Principal Stress Contour Plot of Expected Stress (60deg Load Case).

To reduce the number of nodes and create a more consistent mesh, the small mounting holes on the wheel assemblies were removed during the finite element analysis. Using stress concentration factors, the nominal stress determined in the software was multiplied by the appropriate factor to calculate the adjusted stress. This adjusted stress value was used when comparing against allowable stresses. More information about the stress concentration factors can be found in the Appendix regarding Structural and Mechanical Analysis Process. Below is a Von Mises stress contour plot for the load case resulting in the most severe stresses in the wheel assemblies. The expected stresses are below the allowable stress for the 6061-T6 parent material allowable and result in a passing safety factor of 4.80 compared to the minimum 1.85.

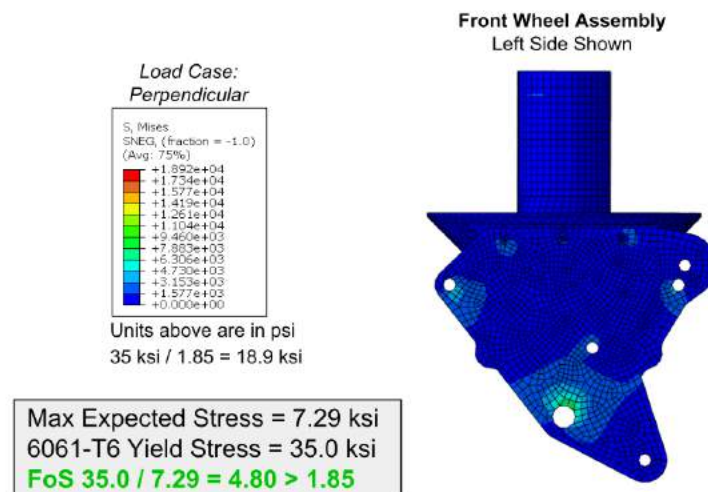


Figure 11. Von Mises Stress Contour Plot of Expected Stress (Perpendicular Load Case).

To accurately analyze the bolted connections, preload values for the structural connections were required. Using Table 7.1 presented in the *Specification for Structural Joints Using High-Strength Bolts* from the Research Council on Structural Connections (RCSC) [9], a quadratic fit was calculated using the documented values, and different bolt pretensions were determined. More information about the bolted preload calculation can be found in the Appendix regarding Structural and Mechanical Analysis Process. The required tensile and resultant shear strengths were extracted from the finite element model beam elements. For conservatism, it was assumed that the maximum shear and tensile forces acted on the same bolt. The equations in the tables below refer to the equations presented in *RCSC Specification for Structural Joints Using High-Strength Bolts 2014*.

Table 5. RCSC Bolt Calculations for 1/4-20 Bolts.

Name	Var	Val	Unit	Comment / Equation	Eqn #
<i>Constants and Factors for Bolted Connection</i>					
Required Tensile Strength	T_u	0.35 kips		Output From FEM Simulation	
Required Shear Strength	V_u	0.37 kips			
Nominal Diameter of Bolt	d_b	0.25 in		Defined by CAD Geometry	
Clamped Material Thickness	t	0.19 in			
Hole Clearance Distance	L_c	0.06 in		RCSC Specified, Except for Slip Critical	
Resistance Factor	Φ	0.75			
<i>Shear and Tension Check</i>					
Nominal Strength per Unit Area	F_{n-Ten}	90 ksi		Values Referenced in Table 5.1	
Nominal Strength per Unit Area	$F_{n-shear}$	54 ksi			
Bolt Cross-sectional Area	A_b	0.05 in ²		$= (\pi / 4) * d_b^2$	
Nominal Tensile Strength of Bolt	R_{n-Ten}	5.89 kip		$= F_{n-Ten} * A_b / \Phi$	(5.1)
Nominal Shear Strength of Bolt	$R_{n-shear}$	3.53 kip		$= F_{n-shear} * A_b / \Phi$	(5.1)
Resulting Tension Safety Factor	$X_{Tension}$	16.7 > 1.67		$= R_{n-Ten} / T_u$	
Resulting Shear Safety Factor	X_{Shear}	9.6 > 1.67		$= R_{n-shear} / V_u$	

Table 6. RCSC Bolt Calculations for 1/4-20 Bolts (Continued).

Name	Var	Val	Unit	Comment / Equation	Eqn #
<i>Combined Shear and Tension Check</i>					
Design Strength in Tension	$(\Phi R_n)_t$	4.42 kip		$= R_n-Ten / T_u$	
Design Strength in Shear	$(\Phi R_n)_v$	2.65 kip		$= R_n-shear / V_u$	
Limit-State of Bolt Configuration	L_{comb}	0.03		$= [T_u / (\Phi R_n)_t]^2 + [V_u / (\Phi R_n)_v]^2$	(5.2)
Resulting Combination Margin	X_{comb}	38.9 > 1.67		$= 1 / L_{comb}$	
<i>Bearing Strength Calculations</i>					
Tensile Strength for 6061-T6	F_u	35.0 ksi		Yield Material in Bearing	
Capacity of Material (Lowest Factor)	R_{cap}	3.28 kip		$= 2 * d_b * t * F_u$	(5.5)
Required Bolt Load (Highest Factor)	R_n	0.62 kip		$= 1.5 * L_c * t * F_u$	(5.4)
Resulting Combination Margin	$X_{bearing}$	5.3 > 1.85		$= R_{cap} / R_n$	
<i>Slip Critical Connection</i>					
Resistance Factor for Slip Critical	Φ	0.85		Specified RCSC Section 5.4.1	
Mean Slip Coefficient	μ	0.33		Assume Lowest Slip Coefficient	
Pretension Multiplier	D_u	1.0		Assume Bolt Pretensioned to Minimum	
Number of Bolts in Joint	N_b	1		Assume Load on One Bolt	
Specified Minimum Pretension	T_m	1.60 kip		Interpolated From Table 7.1	
Nominal Slip Resistance of Plane	R_n	0.41 kip		$= \mu * D_u * T_m * N_b [1 - T_u / (D_u T_m N_b)]$	(5.6)
Resulting Slip Critical Margin	X_{slip}	1.1 > 1.0		$= R_n / V_u$	

Mechanical Analysis

The mechanical components were analyzed for full-load, full-performance operation as well as system abuse and impact while patrons are getting on and off the system. The component calculations were completed assuming all of the system and patron weight are applied to only one wheel assembly. This type of loading is unlikely and will therefore be considered conservative. All of the loads are derived assuming the system will accelerate and perform at the proposed 1g rate. Important factors are listed below:

- A 2.0 Impact Factor was used in many cases for system abuse

The expected forces and stresses and corresponding safety factors for the mechanical components are listed in **Table 7**. The analysis was divided into various components including bearings, shafts, bolts, and belts. All analyzed components meet the required allowables.

Table 7. Safety Factor Summary by Load Case - Mechanical.

Component	Specification	Allowable	Expected	Expect SF	Required SF
<i>Radial Bearing Yaw Shaft</i>	Force Margin	2.63 kip	1.5 kip	1.78	> 1.00
<i>Thrust Bearing Yaw Shaft</i>	Force Margin	11.6 kip	0.6 kip	19.3	> 1.00
<i>Radial Bearing Wheel Shaft</i>	Force Margin	405 lbs	300 lbs	1.35	> 1.00
<i>Timing Belt</i>	Force Margin	750 lbs	587 lbs	1.28	> 1.00
<i>Wheel Shaft Shoulder Bolt</i>	Axial Stress	160 ksi	102 ksi	1.57	> 1.00
	Shear Stress	160 ksi	6.0 ksi	26.8	> 1.00
	Bearing Stress	54 ksi	7.4 ksi	7.33	> 1.85
<i>Motor Bolts</i>	Shear Stress	500 MPa	17.9 MPa	27.9	> 1.00
	Bearing Stress	372 MPa	47.9 MPa	7.78	> 1.85

Each assembly includes two radial bearings pressed into the wheel hub and another radial bearing pressed into the timing belt pulley (enveloped in the following calculations). Using bearing cutsheets available online, the expected forces through the bearings were compared to the rated allowables. All bearing force margins were calculated considering a 300lb patron moving at the maximum acceleration, and in the most severe direction, in order to react the forces on one wheel assembly.

Table 8. Bearing Calculations and Resulting Force Margins.

Force Margin for Bearings				
Name	Var	Val	Unit	Comment / Equation
<i>Rotating Yaw Shaft - Radial Bearing</i>				
Max Expected Load on Bearing	P_{Expect}	1.48 kip		Reaction Force on Lower Bearing
Allowable Load on Bearing (KN)	P_{Allow}	11.7 KN		VXB F6910ZZ Static Load
Allowable Load on Bearing (lbs)	P_{Allow}	2.63 kip		Conversion to Imperial Units
Resulting Force Margin	X_{Thrust}	1.78		$= P_{\text{Allow}} / P_{\text{Expect}}$
<i>Rotating Yaw Shaft - Thrust Bearings</i>				
Maximum Patron Load	W_{Patron}	300 lbs		Max Patron Allowable
Abuse Loading Factor	f_{Abuse}	2.0		Conservative Impact Factor
Max Expected Load on Bearing	P_{Expect}	0.60 kip		$= W_{\text{Patron}} * f_{\text{Abuse}} / 1000$
Allowable Load on Bearing (KN)	P_{Allow}	51.6 KN		Koyo NRB NTA-5266 Dynamic Load
Allowable Load on Bearing (lbs)	P_{Allow}	11.6 kip		Conversion to Imperial Units
Resulting Force Margin	X_{Thrust}	19.3		$= P_{\text{Allow}} / P_{\text{Expect}}$
<i>Wheel Shaft - Radial Bearing</i>				
Number of Bearings	N_{Bearing}	2		Bearings Pressed into Wheel Hub
Max Expected Load on Bearing	P_{Expect}	600 lbs		$= W_{\text{Patron}} * f_{\text{Abuse}}$
Allowable Load on Bearing (KN)	P_{Allow}	1800 N		AST 71900C Static Load
Allowable Load on Bearing (lbs)	P_{Allow}	404.7 lbs		Conversion to Imperial Units
Resulting Force Margin	X_{Thrust}	1.35		$= P_{\text{Allow}} / (P_{\text{Expect}} / N_{\text{Bearing}})$

An L-Series timing belt was used for the propulsion system (shown in purple below). The belt will be tensioned by rotating the motor mount plate away from the wheel. The wheel pulley is attached to the wheel through six bolts to transfer the torque. By using the maximum expected load on the wheel as well as the maximum acceleration, the load through the timing belt could be calculated.

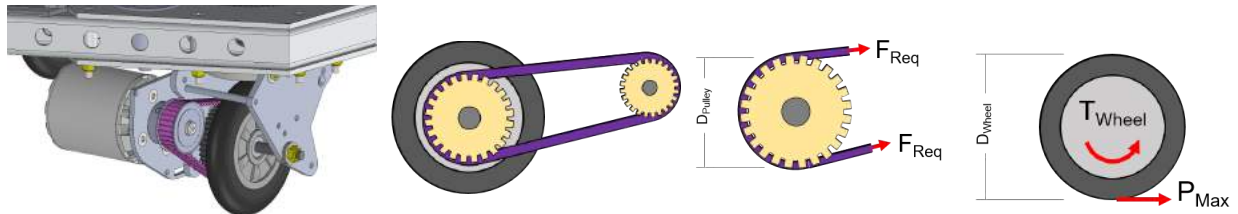


Figure 12. View of Drive Pulley (Left) and Diagrams of Pulley-Wheel Interfaces Components Removed From View for Clarity.

Using the total weight of the system (300lb patron and 62.5lb vehicle), a conservative force margin in the timing belt was calculated. Since it was assumed that the total weight was on one pulley assembly, the narrow force margin listed to the left is acceptable.

Table 9. Timing Belt Pulley Calculations and Resulting Force Margins.

Force Margin for Timing Belt Pulley				
Name	Var	Val	Unit	Comment / Equation
<i>System Geometry and Belt Specifications</i>				
Maximum Force on Wheel	P_{Max}	362.5 lbs		Weight of System and Patron
Diameter of Wheel	D_{Wheel}	5.0 in		5in Pneumatic Wheel
Diameter of Pulley (mm)		78.4 mm		SDP-SI Pulley Listed Below
Diameter of Pulley (inch)	D_{Pulley}	3.1 in		Convert to Inch Measurement
Belt Breaking Strength (per Width)	F_{Break}	125 lbs/(1/8")		SDP-SI L Timing Belts
Width of Timing Belt	W_{Belt}	0.75 in		SDP-SI L Timing Belts
<i>Resulting Calculations for Timing Belt</i>				
Total Breaking Strength on Belt	F_{Belt}	750.0 lbs		$= F_{Break} * (W_{Belt} / 0.125)$
Effective Torque on Pulley	T_{Wheel}	906.3 in-lbs		$= P_{Max} * (D_{Wheel} / 2)$
Force Required by Belt	F_{Req}	587.2 lbs		$= T_{Wheel} / (D_{Pulley} / 2)$
Resulting Force Margin	X_{Force}	1.28		$= F_{Belt} / F_{Req}$

A 10mm diameter shoulder bolt supported the wheel and pulley assembly. The bolt was secured to the side plates of the wheel assembly and load was transferred through the bearings. The analyzed shaft and assembly view is shown below in **Figure 13**.

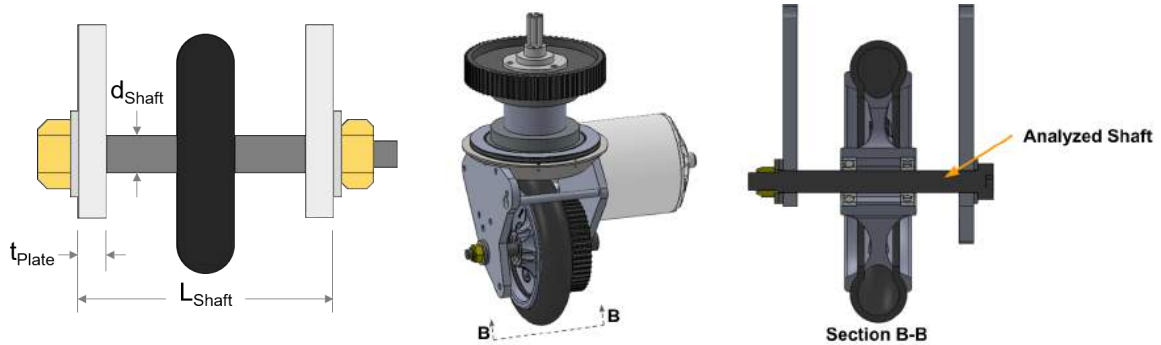


Figure 13. Geometric Diagram (Left), Assembly View (Center), Cross Sectional View (Right).

Using the total weight of the system (300lb patron and 62.5lb vehicle) and an impact / abuse factor, conservative strength safety factors for the wheel shaft were calculated. Considering the bending and shear of the shaft as well as the bearing loads in the plate, the calculated margins are acceptable and the design is sufficient for the expected loads.

Table 10. Drive Wheel Shaft Calculations and Resulting Stress Margins.

Wheel Shaft Strength Calculations				
Name	Var	Val	Unit	Comment / Equation
<i>System Geometry and System Loading</i>				
Shaft Diameter (mm)	d_{shaft}	10 mm		10mm Shoulder Bolt Diameter
Shaft Diameter (in)	d_{shaft}	0.39 in		Conversion to Imperial Units
Unsupported Length	L_{shaft}	3.4 in		Unsupported Length of Bolt
Thickness of Plate Support	t_{plate}	0.25 in		Side Plate Thickness
Total Weight of System	W	363 lbs		Weight of System and Patron
Abuse Loading Factor	f_{abuse}	2.0		Conservative Impact Factor
<i>Aluminum and Bolt Allowables</i>				
Aluminum 6061-T6 Yield Strength	$\sigma_{\text{Alum-Y}}$	35.0 ksi		Referenced in MMPDS
Aluminum 6061-T6 Bearing Strength	$\sigma_{\text{Alum-B}}$	54.0 ksi		Referenced in MMPDS
Class 12.9 Min Yield Strength (MPa)	$\sigma_{\text{Bolt-Y}}$	1100 MPa		Class 12.9 Allowable
Class 12.9 Min Yield Strength (ksi)	$\sigma_{\text{Bolt-Y}}$	160 ksi		Conversion to Imperial Units
<i>Bending Stress in Bolt</i>				
Shaft Moment of Inertia	I_{shaft}	0.001 in ⁴		$= (\pi / 64) * d_{\text{shaft}}^4$
Max Expected Load on Bearing	P_{expect}	725 lbs		$= W * f_{\text{abuse}}$
Max Bending Moment in Shaft	M_{max}	610 in-lbs		$= P_{\text{expect}} * L_{\text{shaft}} / 4$ Simply Support
Bending Stress in Shaft	σ_{bend}	102 ksi		$= M_{\text{max}} * (d_{\text{shaft}} / 2) / (I_{\text{shaft}} * 1000)$
Resulting Factor of Safety	FoS	1.57		$= \sigma_{\text{yield}} / \sigma_{\text{bend}}$
<i>Shear and Bearing Stresses</i>				
10mm Bolt Shear Area	A_{shear}	0.122 in ²		$= (\pi / 4) * d_{\text{shaft}}^2$
Shear Stress in Bolt	σ_{shear}	5.96 ksi		$= P_{\text{expect}} / (A_{\text{shear}} * 1000)$
Resulting Shear Safety Factor	X_{shear}	26.8		$= \sigma_{\text{shear}} / \sigma_{\text{Bolt-Y}}$
Plate Bearing Area	A_{bearing}	0.098 in ²		$= d_{\text{shaft}} * t_{\text{plate}}$
Bearing Stress in Plate	σ_{bearing}	7.37 ksi		$= P_{\text{expect}} / (A_{\text{bearing}} * 1000)$
Max Bending Moment in Shaft	X_{bearing}	7.33		$= \sigma_{\text{bearing}} / \sigma_{\text{Alum-B}}$

The torque required from the motor will be reacted by the bolts mounted to the motor plate. Assuming the torque is reacted equally to all bolts in the bolt pattern, the resultant load per bolt can be calculated. The shear stress in the bolt and the bearing stress in the plate were analyzed and compared to allowables.

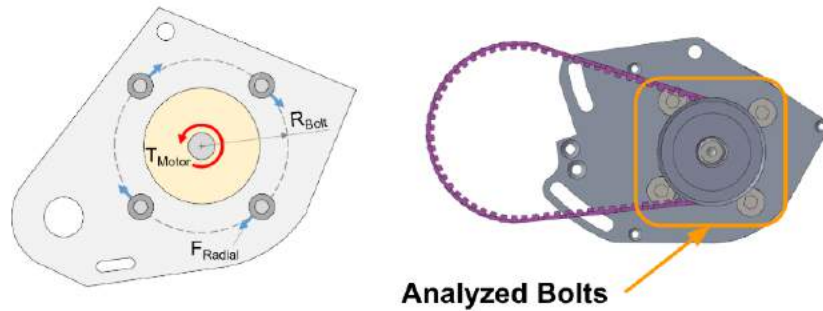


Figure 14. Geometric and Force Diagram (Left) and Assembly View (Right)
Components Removed From View for Clarity.

Since it was again assumed that all of load was being transferred through one wheel assembly, a conservative calculation for the motor bolts was completed.

Table 11. Motor Bolts Calculations and Resulting Stress Margins.

Motor Bolts Strength Calculations				
Name	Var	Val	Unit	Comment / Equation
<i>System Geometry and Allowable Strengths</i>				
Motor Bolt Diameter	d_{Bolt}	6 mm		Bolts Used to Mount Motor
Bolt Pattern Radius	R_{Bolt}	28 mm		Center to Center Distance
Engaged Length of Bolt	L_{Bolt}	1.8 mm		Thickness After Countersink
Diameter of Motor Pulley	D_{Pulley}	43.4 mm		SDP-SI Timing Belt Pulley
DIN 965 Bolt Tensile Strength	$\sigma_{\text{Bolt-T}}$	500 MPa		Referenced Bolted Allowable
6061-T6 Bearing Strength (ksi)		54 ksi		Referenced in MMPDS
6061-T6 Bearing Strength (MPa)	$\sigma_{\text{Alum-B}}$	372 MPa		Conversion to Metric Units
<i>Effective Forces on Motor Bolts</i>				
Force Through Belt (lbs)		587 lbs		Weight of System and Patron
Force Through Belt (N)	F_{Req}	2612 N		Conversion to Metric Units
Expected Torque on Motor	T_{Motor}	56,695 N-mm		$= F_{\text{Req}} * (D_{\text{Pulley}} / 2)$
Radial Loads on Bolts	F_{Radial}	2025 N		$= T_{\text{Motor}} / R_{\text{Bolt}}$
<i>Resulting Safety Factors for Bolts and Aluminum</i>				
Shear Area on Single Bolt	A_{Shear}	28.3 mm ²		$= (\pi / 4) * d_{\text{Bolt}}^2$
Shear Stress in Bolt	σ_{Shear}	17.9 MPa		$= (F_{\text{Radial}} / 4) / A_{\text{Shear}}$
Resulting Shear Safety Factor	X_{Shear}	27.9		$= \sigma_{\text{Bolt-T}} / \sigma_{\text{Shear}}$
Bearing Area on Single Bolt	A_{Bearing}	10.6 mm ²		$= d_{\text{Bolt}} * L_{\text{Bolt}}$
Bearing Stress in Plate	σ_{Bearing}	47.9 MPa		$= (F_{\text{Radial}} / 4) / A_{\text{Bearing}}$
Resulting Bearing Safety Factor	X_{Bearing}	7.78		$= \sigma_{\text{Alum-B}} / \sigma_{\text{Bearing}}$

All of the analyzed components passed the structural and mechanical criteria with sufficient margins for stress and force. The analysis methodology and results were reviewed by an internal and external review panel, and the results were deemed admissible.

Manufacturing Process

Critical Path to Manufacturing Success

Due to the stakeholders desire for a compact, lightweight, yet performance driven vehicle, these constraints led to most of the mechanical components either needing custom machining from stock metal or modifying COTS parts. A wide array of manufacturing processes were utilized throughout the construction of the vehicle including 5-axis waterjet cutting, three dimensional CNC milling, Aluminium welding, as well as manual lathe and milling processes. In order to accurately define a critical path to successful manufacturing, a flow chart was created depicting the order of major milestones. This critical path to success can be seen below in **Figure 15**. and was referred to over the course of the manufacturing process to stay on track in regards to necessary timelines and milestones.

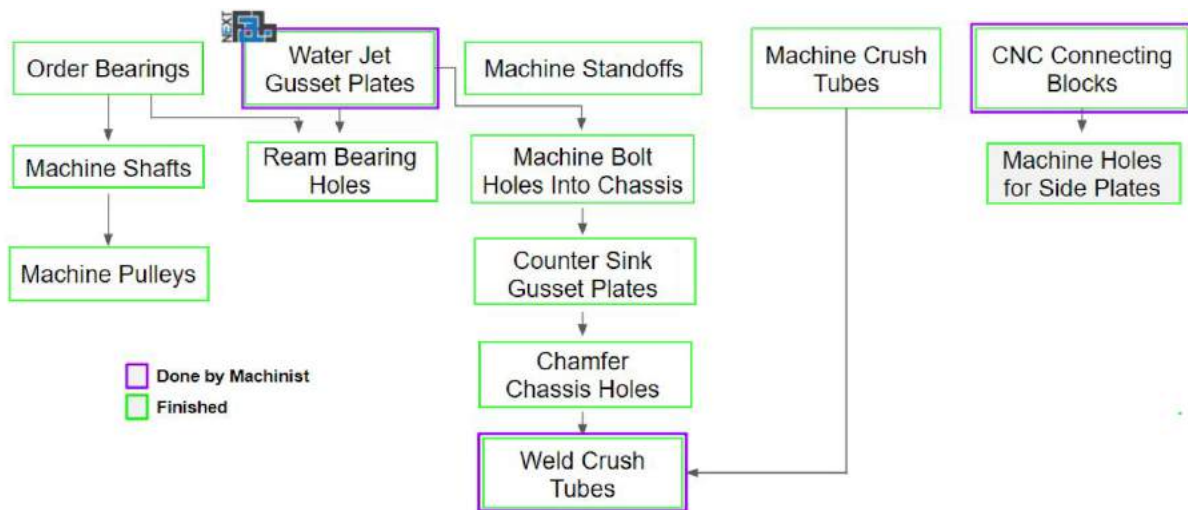


Figure 15. Completed Critical Path to Success for Manufacturing.

To reduce time for manufacturing, many components were designed with specific manufacturing techniques in mind. One of the most important examples of this is the design for waterjet cutting. More specifically, the wheel assembly structure was designed so that the majority of the structure is two dimensional complex shapes joined by standoffs. This type of design is easy to manufacture with waterjet cutting technology, easy to assemble, as well as incredible strong.

As requested by the stakeholder, detailed pictures of every manufacturing process was taken and documented throughout the critical path. A brief overview of the manufacturing methods for each major component of the vehicle will be outlined below.

Gusset Plates

The gusset plate manufacturing involved a mixture of waterjet cutting and manual milling techniques. Two dimensional drawings were first created from the three dimensional engineering models and were given to staff at the NextFab manufacturing facility in Southern Philadelphia. From there the necessary tool paths were generated. The staff at NextFab walked the team through the waterjet cutting process, and in great detail described the operation and fundamental concepts behind the manufacturing procedure. A detailed view of the waterjet cutting gusset plates seen below in Figure 16 as well as the finished parts after waterjet cutting.

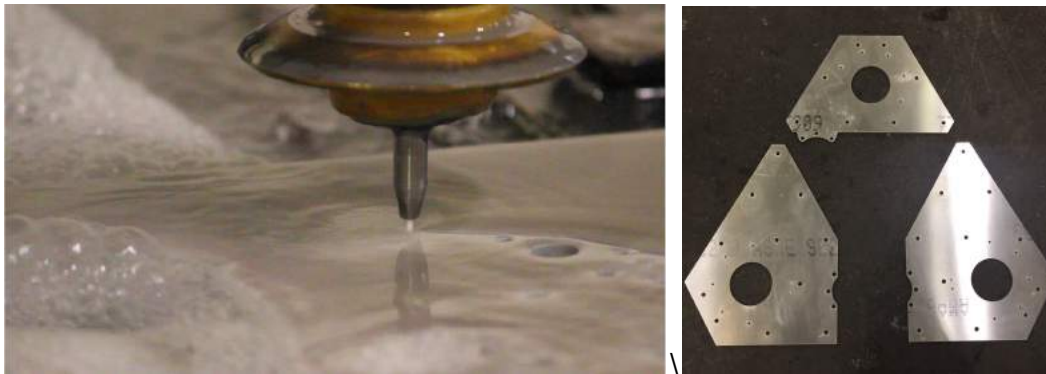


Figure 16. View of Waterjet Cutting Gusset Plates (Left), Plates Post Waterjet Cutting (Right).

The large holes inside the gusset plates for the flange bearings to be press fit into were intentionally undersized for two reasons: the waterjet cutting process left an undesirable surface finish, and the hole needed to be a very precise (within a few thousandths of an inch) in size in order for the flange bearing to correctly sit inside the gusset plate without having any room to shift or move in place.

The post processing technique for these precision sized holes can be seen below in **Figure 17**. Each gusset plate was mounted to a vertical milling machine, and a Coaxial Centering Indicator was used to accurately find the center of the waterjet cut hole (**Figure 17** left). Once the center was found, a boring head with carbide tipped boring bar was mounted onto the spindle (**Figure 17** center). This boring head allowed for the diameter of the circle to be increased at 0.001" increments until the hole was just large enough to allow the flanged bearing to slide into the gusset plate easily but also without the bearing being able to shift or move in place inside the gusset plate hole (**Figure 17** right). This process was slow since great caution needed to be taken due to the fact that no spare gusset plates were manufactured.



Figure 17. Finding Hole Center (Left), Boring Size of Hole (Center), Test Fit Hardware (Right).

Finally, countersinks were added to allow for the flat head hardware to sit flush to the surface of the gusset plates. A countersinking bit was used on a drill press at very low speeds (<400 rpm) to reduce any possibility of bit chatter and create a very smooth surface finish.

Chassis Hollow Structural Tubes

The hollow structural sections of tube were machined from 6061-T6 Aluminum tube stock. A mechanical drawing was produced specifying the dimensions of each member of tube (**Figure 18** left), from which a tape measure was used to mark these dimensions as precisely as possible. A gravity fed, hydraulically controlled, horizontal metal band saw was utilized to rough cut the members of tubes, and a belt sander was used to bring down the dimensions of the pieces to their final state. Next, the gusset plates were clamped into position on top of the hollow structural tubes, then a center punch was used to mark where to drill holes for the bolts connecting the gusset plates to the structural tubes, this method was chosen to ensure a correct fit despite any tolerance stack-ups that might have skewed overall dimensions. The members were brought to the drill press where the holes for the crush tubes were drilled (**Figure 18** center). An 82 degree countersinking bit was used to create a chamfer on these holes to allow space for welding the aluminum crush tubes into place (**Figure 18** right).



Figure 18. Drawing for Structural Tubes (Left), Drilling Holes for Crush Tubes (Center, Right).

The crush tubes were cut to size from tube stock on a manual lathe. The crush tubes and hollow structural tubes were then handed off to the machinists at the Drexel Machine shop for Aluminum welding. The before and after effects of welding the crush tubes into place, as well as the fit check assembly of the chassis can be seen below in **Figure 19**.

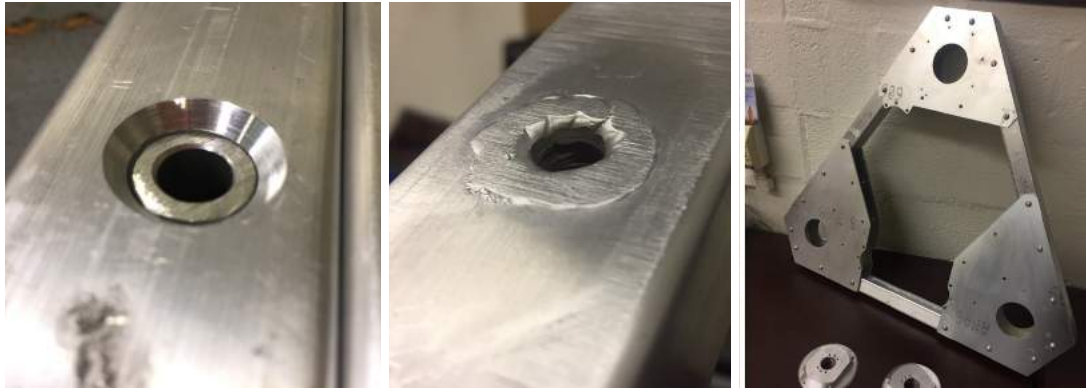


Figure 19. Crush Tube Pre Welding (Left), Post Welding (Center), Assembled (Right).

Shafts

From a manufacturing perspective, the shafts were one of the most labor intensive parts of the whole vehicle. The shafts connect the pulley on top of the vehicle through the two flanged bearings in the gusset plates to the wheel assembly below the chassis and were custom machined from stock 6061-T6 Aluminum. The first step was to mount the stock to a manual lathe and slowly bring down the outer diameter so that it fits inside the inner diameter of the flanged bearing.

Much like the holes in the gusset plates, this dimensions needs to be very precise, thus fit checks were performed every few thousandths of an inch to until the bearing slid onto the shaft easily, but also with as little lateral movement as possible (**Figure 20** left). This process was very slow but yielded a very desirable tight fit. Once the outside diameter was within tolerance, the inside diameter hole of the shaft was manufactured. A countersinking bit was mounted into the chuck on the tailstock of the manual lathe and used to start the hole, then drill bits were used in $\frac{1}{8}$ " diameter increments until the hole was 1" in diameter (**Figure 20** center). A boring bar was then used on the lathe to bring the diameter to it's final 1.18" dimension for the slip ring to fit inside the shaft (**Figure 20** right).



Figure 20. Machining Outside Shaft Dimension(Left), Inside Dimension of Shaft (Center, Left).

Once the outer and inner diameters of the shafts were within tolerance, the parting tool was used on the lathe and the length of the shaft was cut. The shaft was then brought to a manual vertical milling machine with a rotary table attachment where the center of the shaft was located using a Coaxial Centering Indicator (**Figure 21** left). A countersinking bit was then used to start the interfacing holes for the yaw pulley and wheel assembly (**Figure 21** center), then a drill chuck attachment was added to the spindle of the mill and the tap drill size for 10-32 threading was drilled into both sides of the shaft (Fig X right).



Figure 21. Locating Center of Shaft (Left), Starting Holes (Center), Tap Drilling (Right).

Finally, a 10-32 threading was tapped into the six holes on the top and the six holes on the bottom of the shaft (**Figure 22** left). These threaded holes connect to the yaw pulley above the chassis and the wheel assembly below the chassis. The finished part can be seen below in **Figure 22** on the right. A total of 4 shafts were manufactured (1 spare) to account for any manufacturing defects.



Figure 22. Tapping 10-32 Threading into Shaft (Left), Completed Shaft (Right).

Side Plates

The side plates to the wheel mechanism was waterjet cut from 6061-T6 plate, the edge interfacing with the connecting block was purposefully oversized so that it could be precision machined after in order to ensure a smooth surface finish as well as tight tolerance of $\pm 0.005"$. This interface is important to such a tight tolerance since the load path seen below in **Figure 23** is designed to go through the side plate into the connecting block. If the gap is too short then the load path instead travels through the bolts fastening the side plate to the connecting block instead of directly from the side plate to the connecting block.

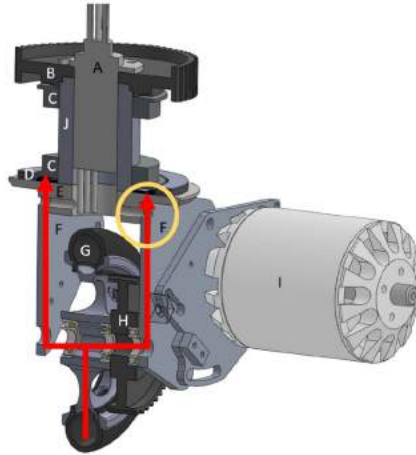


Figure 23. Load Path of Wheel Assembly Mechanism.

In order to ensure this dimension, a solid block of Aluminum was machined flat on a manual milling machine and mounting holes were tapped into the block (**Figure 24** below on the left). Each side plate was mounted to the block using these threaded holes and the hole positions were used to precisely locate the edge of the side plate which was then machined flat with an end mill (**Figure 24** center and right).



Figure 24. Side Plate Fixture (Left), Side Plate Interface (Center), Final Product (Right).

A countersinking bit was then used to add necessary chamfers for flat head hardware, and the side plates were test assembled with the connecting blocks to verify proper dimensions (see connecting block section below).

Connecting Block

The connecting block part required complex geometry in order to act as a connection between the wheel assembly shaft to the waterjet cut wheel side plates of **Figure 25**, which also reducing weight and acting as a mounting and locating surface for the wheel assembly thrust bearing. First the part was imported into Autodesk's Fusion 360 where a computer automated manufacturing simulation was created (seen below in **Figure 25** (left)) . G-code was generated from this simulation and was reviewed by the machinists at the Drexel Machine Shop. After modification of the G-Code, the part was mounted into the CNC mill and manufactured, this can be seen below in **Figure 25** (middle). The final parts were cleaned, deburred, and prepped for further modification, seen below in **Figure 25** (right).

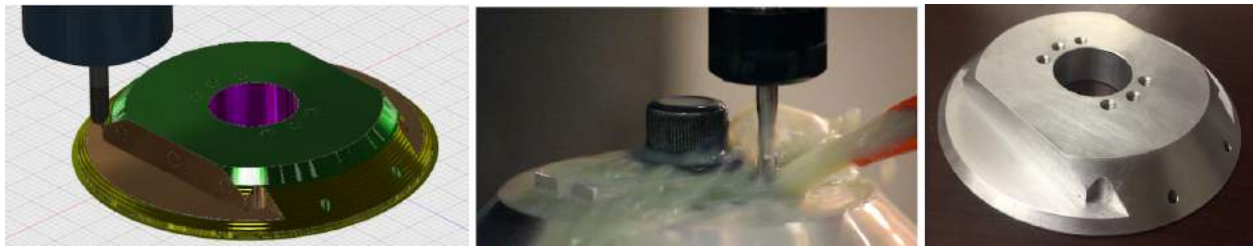


Figure 25. CAM simulation (Left), Actual CNC Machining (Center), Finished Part (Right).

After three dimensional CNC milling, the connecting blocks needed further machining, specifically tapped holes on the side of the blocks that the 3D CNC milling could not achieve in the same pass. These threaded holes were added by mounting the connecting block into the vice on a manual milling machine (**Figure 26** far left). Then locating the part using the specifically designed locating features (**Figure 26** center left). Next a center bit, and tap drill were used to create a hole for tapping the threads (**Figure 26** center right), Finally, a 10-24 tap was used to created the threaded hole which will connect the block to the wheel assembly side plates.

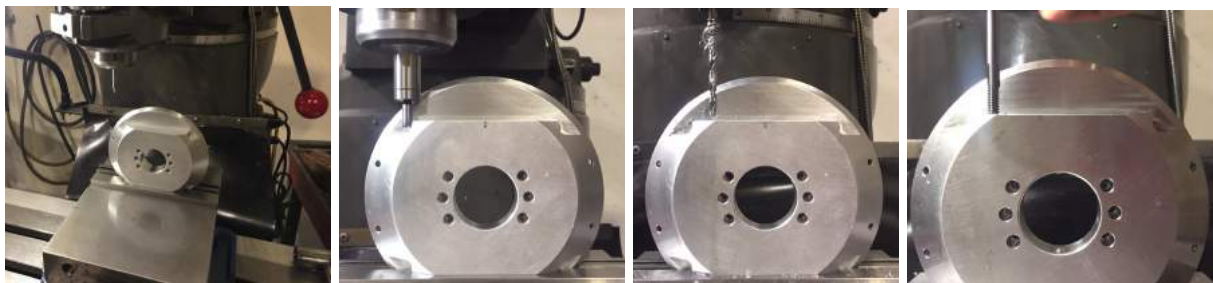


Figure 26. Mounting Block (Left), Locating (Left Center), Drilling (Right Center), Tapping (Right).

Below in **Figure 27** on the left is the test fit with the wheel assembly side plate and on the right side of **Figure 27** is the two wheel assembly side plates and shaft connected to the block.



Figure 27. Test Assembly to Verify Tolerancing (Left), Side Plate, Block, Shaft Assembly (Right).

Wheels

The wheels needed slight modification in order to transfer torque from the propulsion motor pulley to the pulley attached to the wheel. Specifically, a clearance hole pattern needed to be added to the wheel rims in order to attach the pulley to the wheel so that the pulley could transfer torque to the wheel and accelerate the vehicle. This bolt pattern was added to the rim by clamping a rim to a vertical milling machine and using a Coaxial Centering Indicator to locate the rim's center (**Figure 28** left). Next a countersink bit was used to start the hole pattern, and the correct drill bit size was used to create the necessary clearance hole for the 10-32 bolt used to transfer the torque from pulley to wheel (**Figure 28** left center). A 3D printed part was then designed to turn the complex curved surface of the rim to a flat plane in order for the nut which secures the torque transfer bolt to have a flat surface to rest on (**Figure 28** right center). The pneumatic wheel's inner tube and tire were then assembled, the full wheel assembly can be seen in **Figure 28** (right) below.



Figure 28. Locating (Left), Bolt Pattern (Left Center), Nut Mod (Right Center), Assembly (Right).

Pulleys

The yaw motor pulley required a fair amount of custom machining in order to add the required features deemed necessary. The first modification was to enlarge the inner diameter of the pulley to 1.18" in order to fit the slip ring, this was done by stepping up drill bit sizes on the manual lathe until 1" diameter (**Figure 29** left), then a boring bar was used to precisely reach 1.18" diameter (**Figure 29** left center). Next a lip was machined into the bottom of the pulley, this is feature is the same diameter of the shaft and is used to locate the shaft during assembly (**Figure 29** center right). Next the the pulley was clamped to the bed of a vertical manual mill, and the hub used to hold the pulley on the lathe (**Figure 29** right and **Figure 29** left).



Figure 29. Enlarging Dia (Left/Left Center), Adding Lip (Right Center), Mount to Mill (Right).

Once the hub was machined flat, a Coaxial Centering Indicator was used to locate the center of the pulley (**Figure 30** left center) and a clearance hole bolt pattern was machined into the pulley (**Figure 30** right center), this is to transfer the torque from the yaw pulley to the shaft. The fully assembled yaw pulley can be seen in **Figure 30** (right)

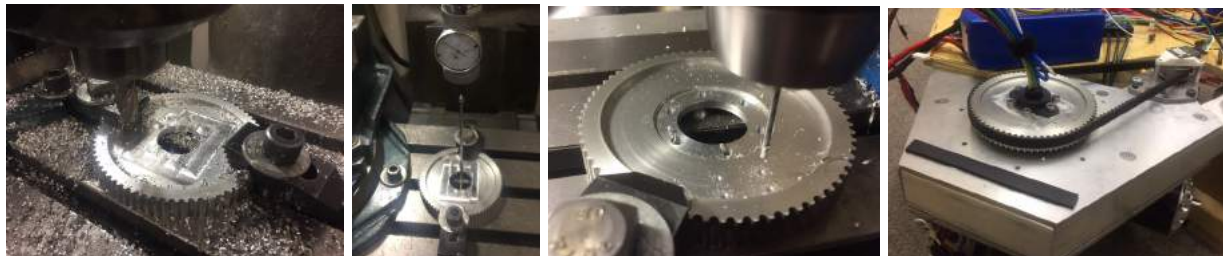


Figure 30. Remove Hub (Left), Locate (Left Center), Pattern (Right Center), Assembly (Right).

The pulleys attached to the wheels seen in **Figure 31** (right) in the wheels sub-section of the Manufacturing Process section of this paper were also COTS but needed modification in order to obtain the desired performance. The modification process started by enlarging the inner diameter of the pulley using an oversized drill bit set on a manual mill, then switching to a boring bar to obtain the precise dimension (**Figure 31** left). The boring bar was then used to create a pocket for the ball bearing that will locate and make the pulley concentric to the wheel assembly axle (**Figure 31** left center). Next the pulley was removed from the lathe and clamped to the bed of a mil (**Figure 31** right center), the hub which was used to hold the pulley on the lathe was then removed using an end mill (**Figure 31** right).



Figure 31. Enlarged (Left), Pocket (Left Center), Mill Mount (Right Center), Removal (Right).

The pulley was then flipped back over and clamped the mill again, where a Coaxial Centering Indicator was used to locate the center of the pulley (**Figure 32** left). Then a countersink bit was used to start the clearance bolt hole pattern which will allow for bolts to transfer the torque to from the propulsion motor to the wheel (**Figure 32** center). The pulley can be seen in the full swerve wheel assembly in **Figure 32** (right) below.

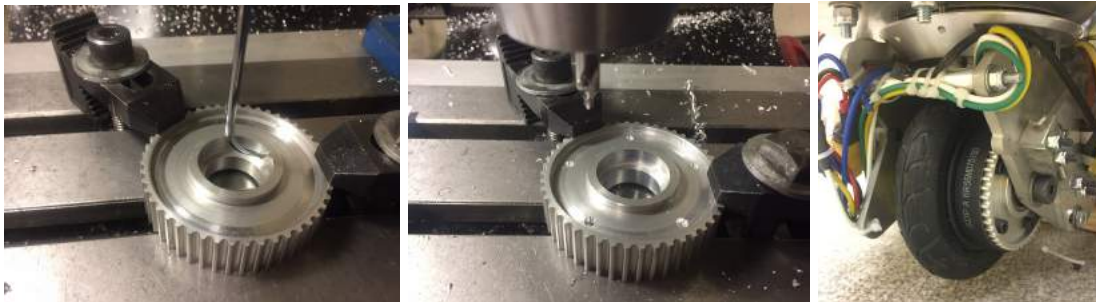


Figure 32. Locating Center (Left), Drilling Hole Pattern (Center), Fully Assembled (Right).

Finally, all pulleys directly mounted to motor shafts needed keyways to be machined into them. Keyways will allow for a much larger amount of torque transfer than a set screw and help achieve the desired performance of the vehicle. The process to add a keyway to a pulley involves using a keyway broaching set. First a collar is placed on the pulley to define the desired orientation of the keyway (**Figure 33** left), next the keyway broach is inserted into the collar (**Figure 33** center), an Arbor Press was used to push the broach down through the pulley which cuts the keyway into the pulley (**Figure 33** right).



Figure 33. Broach Collar (Left), Broach Setup with Press (Center), Close up of Broach (Right).

If need be, a shim was added and the broaching process was repeated until the keyway depth was of the desired dimension (**Figure 34** left). Next the key was inserted into the motor shaft (**Figure 34** center), and the pulley was assembled onto the motor shaft (**Figure 34** right).



Figure 34. Pulley and Keyway Broach (Left), Motor and Key (Center), Fit Keyed Pulley (Right).

Electronics

Electronics Selection Overview

The selection for the electronics was determined based on the selection provided by the stakeholder and the requirements determined by the software architecture. The stakeholder previously purchased and provided the six brushless DC (BLDC) motors used on the platform (three motors to drive the wheels, three motors to drive the yaw pulley) along with six BLDC motor controllers called VESC and magnetic robot encoders. An onboard computer with an operating system was required to setup the ROS network for the platform software to be operate. Microcontrollers are used to provide real time control over the motors through their motor controllers while also being able to receive/send data to and from the onboard computer. A human machine interface device is also required to allow the platform operator to control the platform.

The electronics previously mentioned are all that is necessary to be able to control the platform as desired by the stakeholder. Additional electronics were implemented onto the platform to provide additional sensing in the case the platform was used for robotics research or autonomy.

Computing Hardware

An UpBoard Squared Single Board Computer (SBC) was used as the central onboard computer since this board comes with up to 8GB of system memory and 64GB of system capacity. Additionally this board comes with a 2.5GHz Intel processor which provides more than enough computing power required for teleoperation of the platform while also providing additional available processing power for more computationally intensive tasks like autonomy.

Teensy 3.6 microcontrollers were used to bridge the communication from the onboard computer to the motor drivers. The Teensy 3.6 is a 3.3V 180 MHz ARM processor, 2 CAN Bus ports, 14 hardware timers, along with a large amount of other features that all fits within a footprint that less than half the size of an Arduino. Additionally, this microcontroller is Arduino compatible allowing it to utilize any code written for the Arduino ecosystem and can be programmed using the Arduino IDE. This decreases development time due to the large support community around the Arduino ecosystem and the tools provided with the Arduino IDE.

Actuators

The platform comes with one yaw motor and one drive motor that is placed on each wheel assembly. The yaw motor is responsible for actuating the wheel assembly while the drive motor is responsible for actuating the wheels. The yaw motor is a 63mm 190KV brushless DC motor and the drive motor is a 80mm 50KV brushless DC motor, both from Alien Power Systems. The yaw motor is rated up to 80A while the drive motor is rated up to 200A. These motors were previously purchased and provided by the stakeholder for use on the platform.

Sensing

The platform comes with a AS5047 14-bit magnetic encoder (16384 counts per motor shaft revolution) on each wheel. This encoder works natively with the VESC BLDC motor controller and provides highly accurate absolute positioning of the motor shaft that is used to perform position and velocity control. The drive motor actuates the wheel through a belt drive with a 8:5 gear ratio providing the drive motor with 26214.4 counts per revolution or a resolution of 0.0137 degrees. Additionally, the yaw motor actuates the wheel assembly through belt drive with a 35:9 gear ratio providing the yaw motor with 63715.5 counts per revolution or a resolution of 0.00565 degrees.

Calibration Block

In order to find the position of the wheel assembly, a calibration feature was added to the yaw pulley. This is required since the gear ratio between the yaw motor and yaw pullet is not 1:1. This will be used to ensure each of the wheel assemblies are oriented in the correct direction.

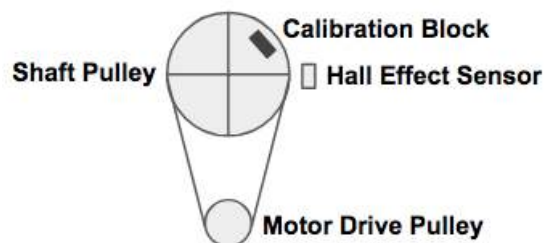


Figure 35. Calibration Block Diagram.

Additionally, the platform is setup to work with the SICK TiM561 2D scanning LiDAR, Stereolab ZED stereo camera, and a Bosch BNO055 IMU. The TiM561 is used for mapping and localization when running the platform in autonomy mode, the ZED camera is used for obstacle avoidance and feature detection that can also be used for six degree of freedom motion tracking, and the BNO055 IMU provides platform acceleration, angular speed, and orientation.

Motor Control

VESC BLDC motor controllers were used to actuate both the yaw and drive motors. This motor controller comes with integrated motor calibration, motor control (position and velocity), encoder interfaces, communication interfaces, battery limiting features, and other integrated tools and settings. This controller incorporates all of the motor control features required to run the platform allowing for processing power required for motor control to be offloaded onto a separate device.

The yaw motor VESC's will be placed in position control to ensure each of the wheel assemblies are oriented in the correct direction to ensure the platform does not try to pull itself apart due to a wheel misalignment. Additionally, each wheel motor VESC will utilize velocity control.

Safety Features

The platform comes with a mechanical kill switch that acts like a rip cord that can be found in boats. If the cord is pull off the switch, all devices connected to the switch are powered off. This switch is connected in series between the electronics battery and all of the electronics excluding the VESC's. In the case the kill switch is activated, the onboard computer, microcontrollers, and sensors (other than the encoders) will be powered off and will be break communication between the microcontrollers and the motor controllers. The VESC's are setup to provide current braking to the motors in the case it loses communication with the microcontrollers for more than 250ms.

Electronics Layout

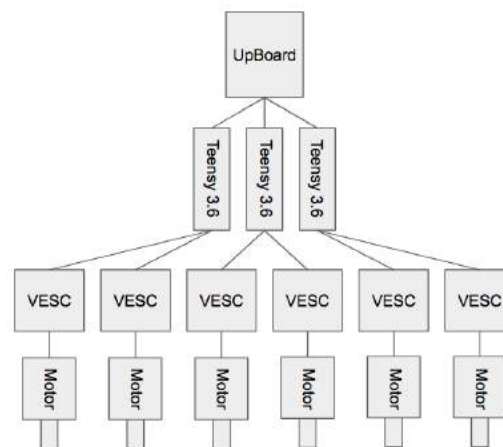


Figure 36. Simplified Electronics Layout.

Figure 36 above shows the layout of the electronics mentioned above.

Software

Software Architecture Overview

The software was designed in consideration of the following elements:

1. The platform will not be manufactured/assembled until near the end of project timeline
2. Specific software implementations may change during the course of the project

For these reasons, software for the robotic platform was designed in order to provide an interface for both a simulated robot and existing robot and was designed through sets of packages in order to allow changes for some of the concepts developed earlier on in the project that are subject to change. The software also should be consistent between using data generated from a simulated platform and the existing platform so that changes made to the software are not affected by either of the simulations but work seamlessly with both.

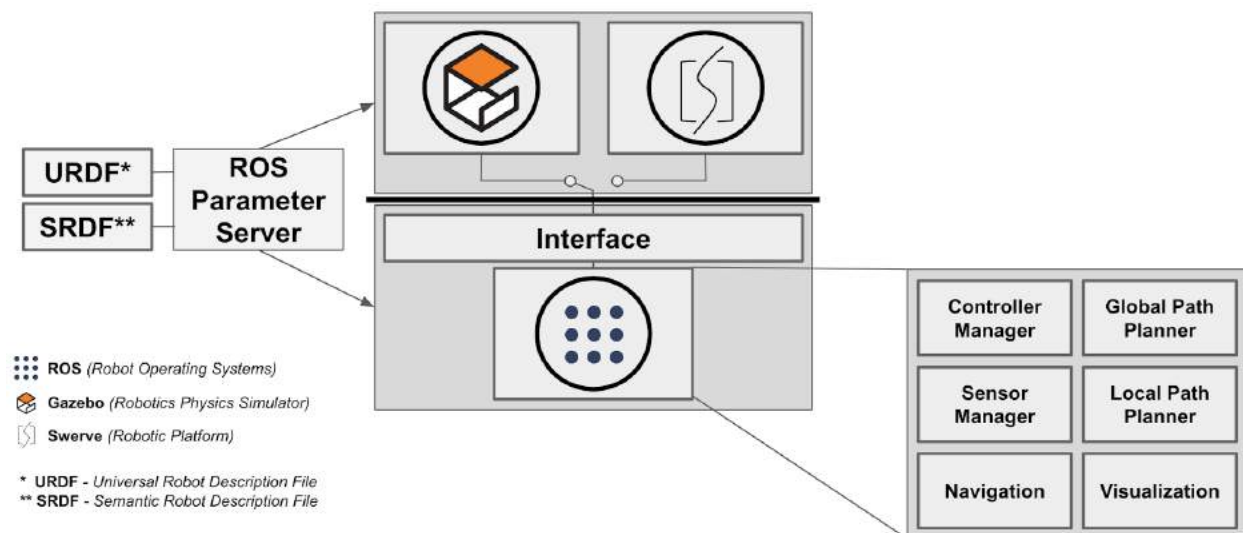


Figure 37. Software Architecture Visual Depiction.

Figure 37 above shows the elements of the software framework that were developed for the platform. A set of six packages are provided with the software in order provide interfaces to all the electronics, motors, and sensors along with visualizations and autonomy. In the case the customer desires for either manual or autonomous control of the robot, none of the packages need to be removed but rather a higher level setting can be provided to the platform in order to change the operation mode. Additionally, if the customer would like to simulate the platform instead of running an existing platform, a visual robotics physics simulator can be used that mimics all the mechanical and software properties of the platform operating in the real world, which can be used to test additional software or sets of operations before running it on the existing platform.

Software Development Tool Utilization

The software for the platform was developed in a framework called ROS (Robot Operating Systems) which acts as middleware on a Linux operating system. ROS runs as a distributed systems of nodes that can communicate with each other across a single processor or multiple processors. ROS also provides many useful tools and packages that allow the accelerated development time and decreases the amount of time debugging. There is extensive documentation and a large support community online for ROS which is largely beneficial when developing software for a platform with a small software development team. ROS is compatible with many popular and third-party softwares including MATLAB and the Gazebo physics simulator while provides and additional range of tools for software development.

Robot Frame Definitions

Figure 38 below shows the frame definitions of the robot that is used for simulating the platform along with visualizations. The *odom* frame is the base frame of the robot located on the floor (when the platform is on the ground) aligned with the geometric center of the platform. The six degree of freedom location of this frame is provided either by the onboard autonomy package or an external sensing system like a motion capture facility. This frame is aligned with the x-axis oriented in the forward direction of the platform and the z-axis oriented away from the ground as is commonly done in ground robotic platforms. The *body* frame is located at the geometric center of the chassis elevated in the z-direction from the *odom* frame at the center of the platform chassis in the z-direction. There are three frames that are have a fixed position and orientation to the *body* frame along with six frames that are actuated by motors (three motors for actuating yaw on the wheel assemblies and three motors to actuate the wheels). Each of the motor frames are set to have one degree of freedom since each of the joints actuated by the motors only provide one degree of freedom movements.

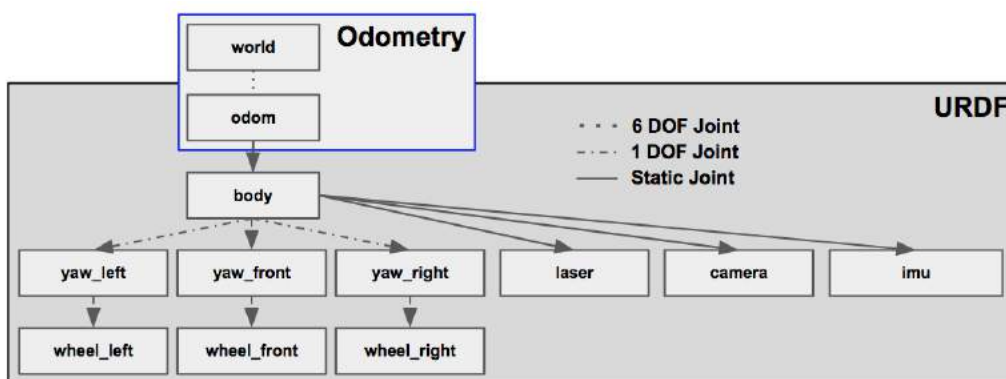


Figure 38. Frame Definition of the Platform.

A visual representation of these frames can be seen in **Figure 39** below which is using a simplified geometric model of the platform.

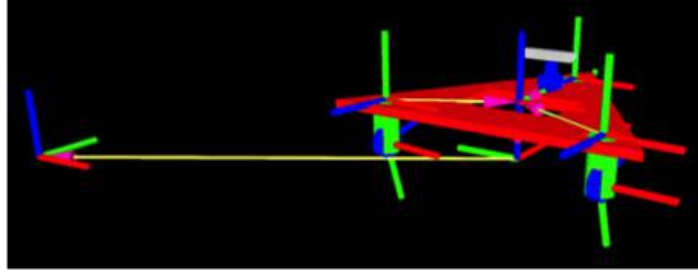


Figure 39. Visual Representation of Platform Frames Using Simplified Geometry.

The location of any of these frames on the robot can then be calculated using a transformation matrix defined by the frame definition, frame location, and the current joint position.

Simulation Environment

As mentioned previously, the platform was simulated using the Gazebo physics simulator in order to test the software architecture and algorithms being implemented on the platform before having the physical platform. Gazebo provides a large range of integrated tools like sensor data simulators and noise models, ground truth odometry, and allows for the user to define mechanical properties like friction and inertia in order to better model the simulated system.

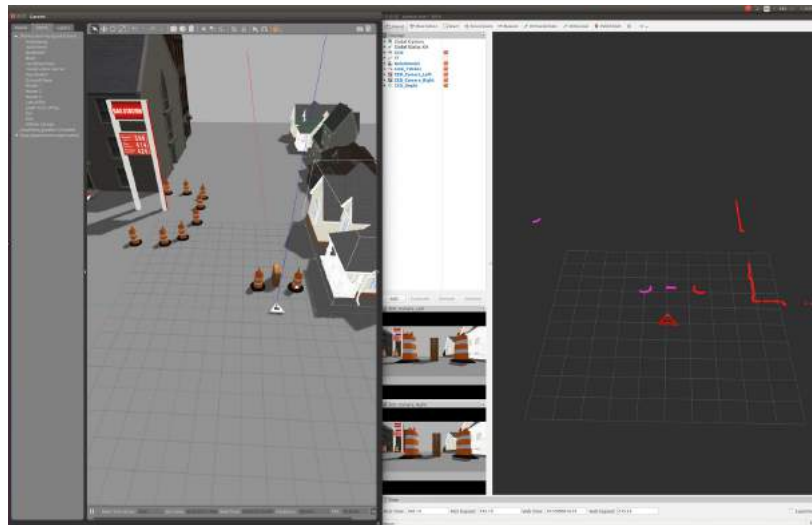


Figure 40. Simplified Platform Simulated in Gazebo (left) and displaying data from ROS (right).

Figure 40 above on the left demonstrates the simplified platform geometry in the Gazebo while window on the right of the image is visualizing the data from ROS using one of its integrated tools. The Gazebo simulator was setup to provide stereo camera data (seen on the bottom middle of the figure), LiDAR data (seen as the red and purple dots in the window on the right), and IMU data (not visualized). As mentioned before, the ROS system is not able to differentiate if the data it is receiving is simulated or coming from sensors on the real platform. The simplified platform can then be controlled in Gazebo and data generated from the simulator would then be provided to the ROS network in order to test the software and algorithms.

Communication Protocols

The communication protocols used include TCP/IP, CAN, and UART. TCP/IP is used within the ROS network in order to communicate amongst the various nodes throughout the network. This network and network tracking is automatically setup through the ROS core node which is started by the user. The CAN and UART protocols can be used to communicate between one of the microcontrollers and a motor driver. **Figure 41 to 43** outline the protocol structure.

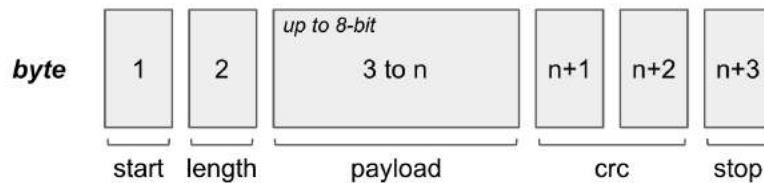


Figure 41. Protocol for UART Communication with VESC using an 8 bit payload.

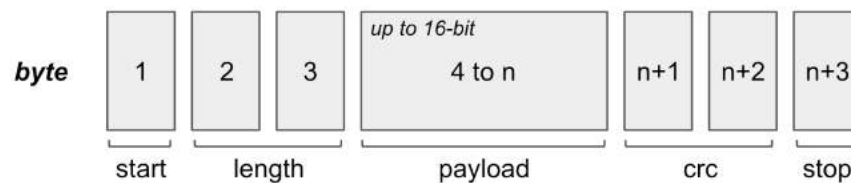


Figure 42. Protocol for UART Communication with VESC using a 16 bit payload.



Figure 43. Protocol for CAN Communication with VESC.

Software Version Control

Git is a UNIX was utilized as the software version control tool to keep track of changes, allow for multiple programmers to work on the same portions of the software, issue tracking, and allow for development work to be done without affecting software that is operational. Github is an online tool that was utilized to host all the software remotely and provide interfaces to interact with the features of Git. Below is a link to the Swerve Github organization.

Swerve Github Organization Link: <https://github.com/SwerveRoboticSystems>

Algorithms and Autonomy

Kinematic and Dynamic Modeling

In order to accurately control and predict the motion and feedback of the vehicle, both a kinematic and dynamic model were created. The desired kinematics of the body frame drive the resulting dynamic response of each wheel. Given the vehicle linear velocity state, the vehicle angular velocity state, and the intended radius of curvature pseudo state (calculated internally), the high-level vehicle kinematics are determined and each wheel yaw and propulsion is defined.

List of variables used in equations (1-1) through (1-14):

dt	= Differential Amount of Time
g	= Acceleration due to Gravity
i	= Wheel Iteration (Front, Left, Right)
J	= Rotational Inertia of Wheel Assembly
m	= Total Mass of Wheel Assembly
r_{Curve}	= Radius of Curvature
r_{Geom}	= Wheel Distance From Vehicle Center
v_B	= Translational Velocity of Body
ω_B	= Rotational Velocity of Body
ω_{Yaw}	= Rotational Velocity of Wheel Assembly
α_{Yaw}	= Rotational Acceleration of Wheel Assembly
x_{IC}, y_{IC}	= Instantaneous Center Coordinates
ψ_{Wheels}	= Angle Offset Between Wheels (120deg)
ϕ_{World}	= Angular Position of Body Frame

For a general path, following an instantaneous radius of curvature, the kinematics of each wheel are defined in equations (1-1) through (1-11). This case was considered the most general case in that any other rigid body motion can be derived using this formulation including straight-line travel and translating instantaneous center.

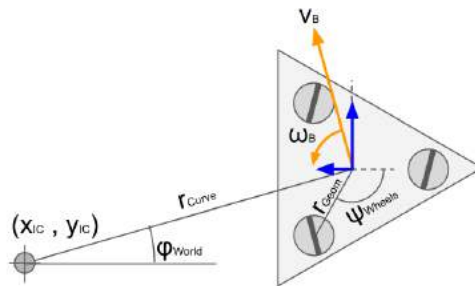


Figure 44. Diagram of Variables for the Kinematic Model.

Calculate translational component of body position

$$x_B = r_{Curve} * \cos([v_B dt] / r_{Curve} + \varphi_{World}) + x_{IC} \quad (\text{EQ 1-1})$$

$$y_B = r_{Curve} * \sin([v_B dt] / r_{Curve} + \varphi_{World}) + y_{IC} \quad (\text{EQ 1-2})$$

Calculate translational component of body velocity

$$v_{x-B} = d/dt(x_B) = -v_B * \sin([v_B dt] / r_{Curve} + \varphi_{World}) \quad (\text{EQ 1-3})$$

$$v_{y-B} = d/dt(y_B) = +v_B * \cos([v_B dt] / r_{Curve} + \varphi_{World}) \quad (\text{EQ 1-4})$$

Calculate position of each wheel given translation and rotation

$$\theta_B = \omega_B dt + \theta_{B-Initial} \quad (\text{EQ 1-5})$$

$$x_i = x_B + r_{Geom} * \cos(\pi/2 + \{i\} \psi_{Wheels} + \theta_B) \quad (\text{EQ 1-6})$$

$$y_i = y_B + r_{Geom} * \sin(\pi/2 + \{i\} \psi_{Wheels} + \theta_B) \quad (\text{EQ 1-7})$$

Calculate velocity of each wheel in the x-axis and y-axis

$$v_{x-i} = v_{x-B} - \omega_{Body} * r_{Geom} * \sin(\pi/2 + \{i\} \psi_{Wheels} + \theta_B) \quad (\text{EQ 1-8})$$

$$v_{y-i} = v_{y-B} + \omega_{Body} * r_{Geom} * \cos(\pi/2 + \{i\} \psi_{Wheels} + \theta_B) \quad (\text{EQ 1-9})$$

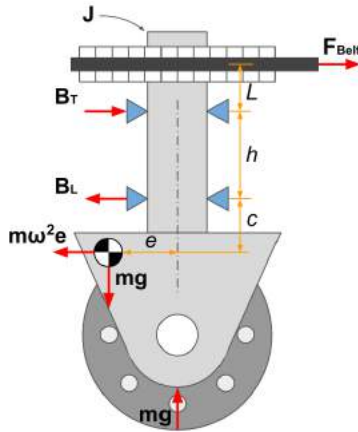
Calculate the yaw and angular velocity of each wheel

Chain Rule for a parametric curve : $(dy/dt) / (dx/dt) = dy/dx$

$$\theta_i = \tan^{-1}(v_{y-i} / v_{x-i}) \quad (\text{EQ 1-10})$$

$$\omega_i = (2/d_{Wheel}) * \sqrt{(v_{y-i})^2 + (v_{x-i})^2} \quad (\text{EQ 1-11})$$

For each wheel assembly, the dynamics of the system were modeled using an energy approach and utilizing the euler-lagrange formulation. Given the system geometry and the various forms of energy, the dynamics are defined in equations (1-12) through (1-14). These equations are used to formulate a solution given an input as a function of yaw angle, $f(\theta)$.



Assume Power Done by Friction: $P = F_f * \text{vel.} = \psi F_N * \dot{\theta}$

Where: F_N = Load on Bearing
 ψ = Proportional Factor

$$\Sigma M: B_L h + mge - F_{Belt} L - m\dot{\theta}e(c + h) = 0$$

$$B_L = [F_{Belt} L + m\dot{\theta}e(c + h) - mge] / h$$

Figure 45. Force Diagram of Wheel Assembly and Resulting Force Calculations.

Determine the energies and Lagrangian of wheel assembly

Lagrangian Defined as : $L = T - U$

$$T = (1/2) * J * \omega_{Y_{aw}}^2 + (1/2) * m * v_{Mass}^2 \quad (\text{EQ 1-12})$$

$$T = (1/2) * J * \omega_{Y_{aw}}^2 + (1/2) * m * \omega_{Y_{aw}}^2 * e^2 \quad (\text{EQ 1-13})$$

Calculate Euler-Lagrange and resulting wheel assembly dynamics

Euler – Lagrange Defined as : $d/dt (\partial L / \partial \dot{g}) - (\partial L / \partial g) = (\partial P / \partial \dot{g})$

$$(J + me^2) \alpha_{Y_{aw}} = -\psi [F_{Belt} L + m \omega_{Y_{aw}} e (c + h) - mge] / h + f(\theta) \quad (\text{EQ 1-14})$$

Laser Scan Matching

The robot receives 2D Light Detection and Ranging (LiDAR) data through a SICK TiM561 sensor represented by scan angles and ranges. Specifically, the sensor scans over 270 degrees. Through successive scans, the relative position change in terms of $(\Delta x, \Delta y, \Delta \theta)$, which are translation in the x and y-direction and rotation, can be estimated using the iterative scan matching algorithm with the Normal Distributions Transform (NDT) [10].

Essentially, the way the scan matching algorithm works is:

1. Build the NDT for the first scan.
2. Initialize estimates for $(\Delta x, \Delta y, \Delta \theta)$ such as zeros or from odometry.
3. Map reconstructed 2D points of the second scan into the first scan coordinate frame.
4. Determine the normal distribution (μ, Σ) for each mapped point based on first scan NDT.
5. Score the parameters by summing the probability for each mapped point.
6. Update new parameter estimates by optimizing the score using Newton's algorithm.
7. Go to step 3 until convergence.

In terms of building the NDT, the algorithm is as follows:

1. Subdivide the 2D space around the robot into equally spaced cells.
2. For each cell with at least 3 points, calculate the mean and covariance matrix (μ, Σ) for the points in the cell.

Using this scan matching algorithm, pose over time can be estimated by accumulating the position changes (translation and rotation) through successive LiDAR scans. In MATLAB, the *matchScans* function, which implements the algorithms in [10], was used. These pose estimates are then used in conjunction with the LiDAR scan angles and ranges to build an estimate of a 2D map, as is discussed in the next section.

Occupancy Grid Mapping

The natural 2D map representation using LiDAR scans are occupancy grid maps. Occupancy grid maps can be visualized as a square grid that has been subdivided with evenly spaced cells of equal length. Each cell edge is represented as a unit of some predetermined distance. The reason that occupancy grid maps work well with LiDAR scans is that a current pose estimate can be associated with some cell block, and free cells and occupied cells can be computed by casting rays from the current pose using the corresponding scan angles and ranges. Therefore, the grid cells that the casted rays land on can be considered occupied, and the grid cells that the rays passed through can be considered free. The potential free cells are determined using Bresenham's line algorithm. Specifically, the free and occupied cells are classified probabilistically using log-odds, which has been extended from [11]. **Figure 46** shows how the log-odds value are updated for each cell in the grid, where 1 represents the cell being occupied and 0 represents the cell being free. Therefore, the more evidence that accrues for a certain grid point, the more that grid point can be trusted as either free or occupied. It can be noted that an accurate occupancy grid map heavily depends on accurate pose estimates. Since rays are casted from the pose estimate, if the pose drifts over time, the map will get distorted as areas of the map that should not have been mapped are denoted as either free or occupied, and cells that have been denoted as free or occupied in the past can get overwritten with the wrong classification.

The occupancy grid mapping algorithm was implemented in MATLAB. An example of using true poses with occupancy grid mapping to construct the 2D map can be seen in **Figure 47**. Another example of doing the same process, however, on data that was recorded with the SICK TiM561 on a mobile robot walking through the hallways of the Main building can be seen in **Figure 48**. In that dataset, some noise was removed by preprocessing with a 1D 3rd order median filter. As can be seen, the occupancy grid map constructed with pose estimates strictly using only scan matching results, resulted in a distorted map. This is due to the errors associated with using the approximation algorithm. Since the translation and rotation computed at each scan are accumulated onto the previous pose estimate, errors start to accumulate over time which result in drift of the position estimate. Additionally, since the scans can contain noise readings, this affects the accuracy of the algorithm. Errors can potentially be corrected for by both further filtering out the noise points in each scan, and using odometry data from encoders to help adjust the pose estimates.

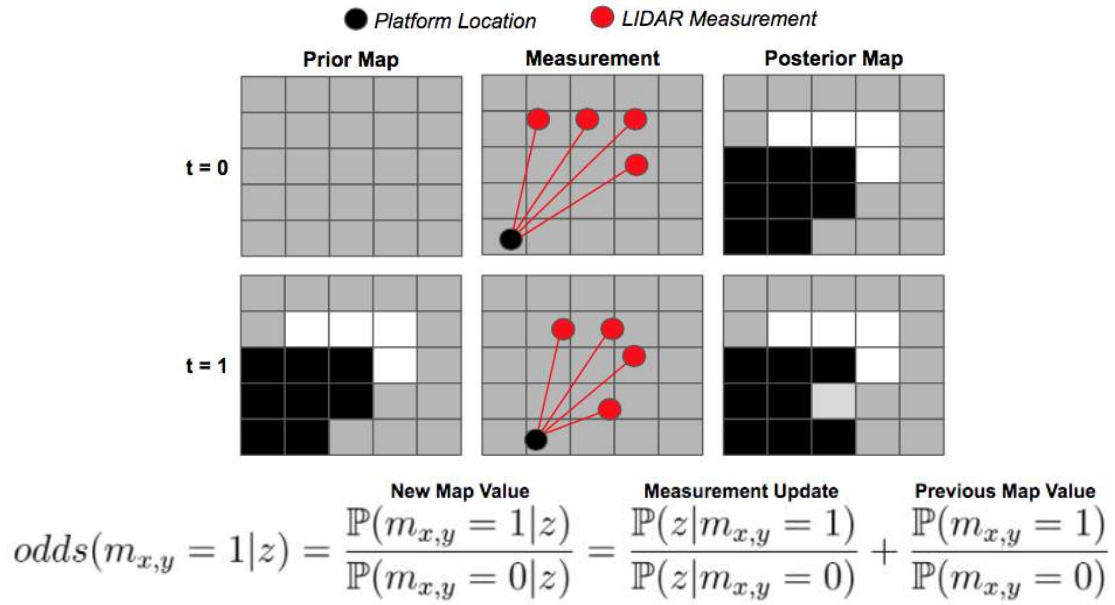


Figure 46. Occupancy Grid Mapping Computations and Visual Depiction.

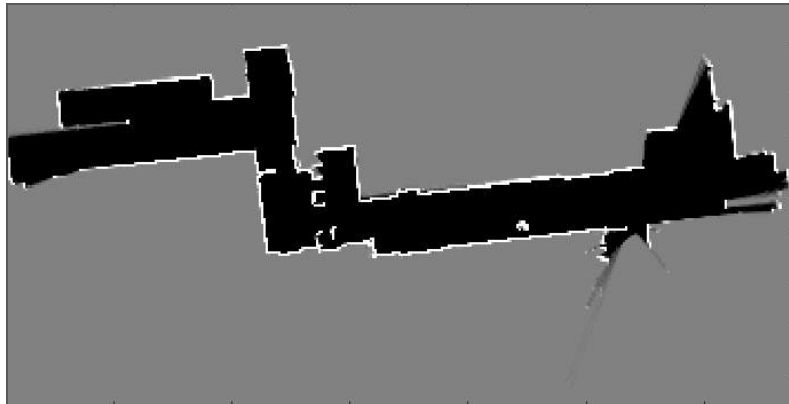


Figure 47. Occupancy Grid Map Built Using Exact Pose and Clean LiDAR Data.

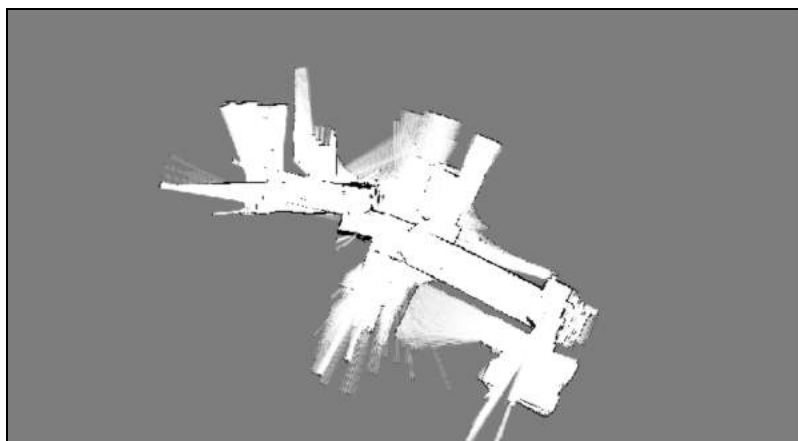


Figure 48. Occupancy Grid Map Using Pose Estimates and Noisy Data.

Particle Filtering

Given a known map, such as the 2D occupancy grid, position over time can be estimated using a particle filter with LiDAR scan angles and ranges. Particle filters have the advantage that the robot's dynamics do not need to be known, and that it makes no linear or Gaussian assumption that the Kalman filter would make. However, if robot dynamic's are known, they can be used in conjunction with the particle filter to give even more accurate states over time with less particles required. Particle filters are a Sequential Monte Carlo technique that simulates by sampling potential states (particles) and weighting those samples in order to approximate [12].

A visual representation of what is happening with a particle filter can be seen in **Figure 49**, where particles are represented by the triangles. In particular, the sampling distribution can be of any distribution that accurately fits the propagation of the system. However, if that is not known it can be assumed to be from a Gaussian distribution of 0 mean and some covariance. Each of these samples or particles represents a potential future state. It is also here that a dynamic model can be used to more accurately propagate potential states. After this, an observation is made from the environment, and the particles are weighted according to how the observations register with the map at that particle. The particle that is weighted with the highest score is taken as the next predicted state. Naturally, if many of the particles score with a low weight, the particles can be resampled according to weight such that the heavier particles reproduce more in the next set of samples, resulting in the genetic algorithm behavior.

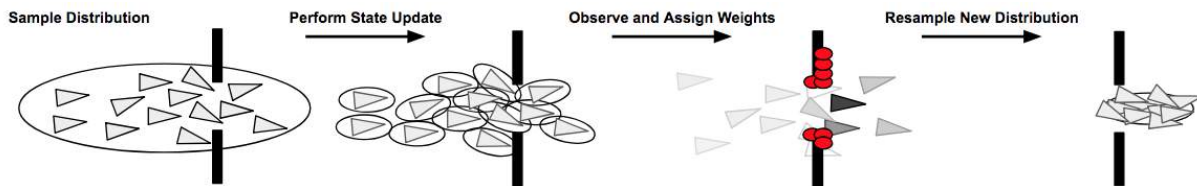


Figure 49. Depiction of State Update Using Particle Filter.

Using the particle filter for position estimates over time makes substantial use of measurements. Therefore, it requires an accurate representation of the map due to map registration with the measurements used when weighing the particles. Thus, the distorted occupancy grid map that was constructed with the errors that accumulated from scan matching as discussed in the previous section would not have made a good map to use for particle filtering. Instead, the particle filter has been coded in MATLAB, and used with new clean LiDAR data on the occupancy grid map that was built with exact poses to estimate position over time from the LiDAR data as can be seen in **Figure 50**.

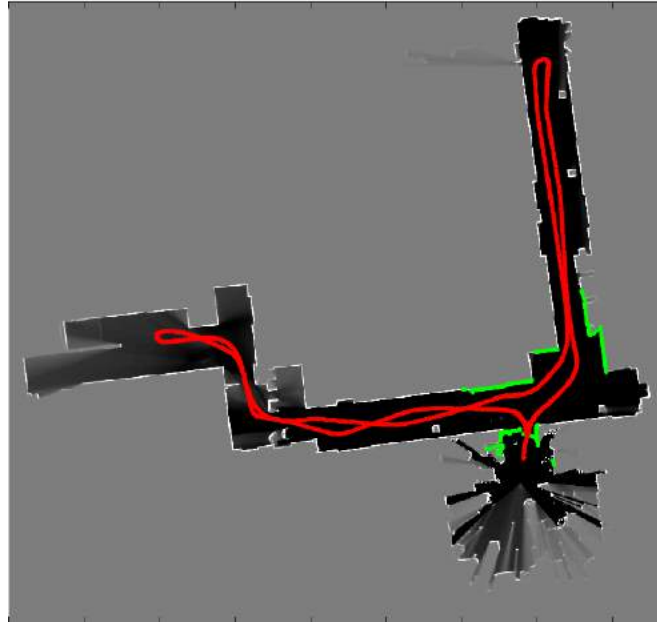


Figure 50. Using Particle Filter to Estimate State Over Time on an Occupancy Grid.

The particle filter could potentially be used on the dataset where the robot moved through the hallways of Main. Better LiDAR data can be collected of less noise by possibly moving slower. Then, further noise would still have to be removed from the data before being run through scan matching. Trusting that the scan matching algorithm produced accurate states, an occupancy grid map can be constructed using those pose estimates, scan angles, and ranges collected. The robot can then be reset to some known starting position in the hallway, and can then run through the same environment to collect new LiDAR data. This LiDAR data can be put into the particle filter algorithm to estimate the position of the robot over time.

Path Planning

With a known map, such as an occupancy grid, and the ability to track the position of the robot over time, paths can be constructed and provided to the platform for autonomous operation. Valid paths can be generated using algorithms like A* which search through the known map for valid paths from the robot location to an end location and use a set of heuristics in order to determine the “optimal” path based on the sample paths that were generated. The robot can then follow this path in an open-loop manner in order to reach the end location autonomously. **Figure 51** shows a valid optimal path generated in MATLAB using the A* algorithms with a known map. Obstacles are represented in red with the robot location starting in the top left cell and the end location in the center of the map.

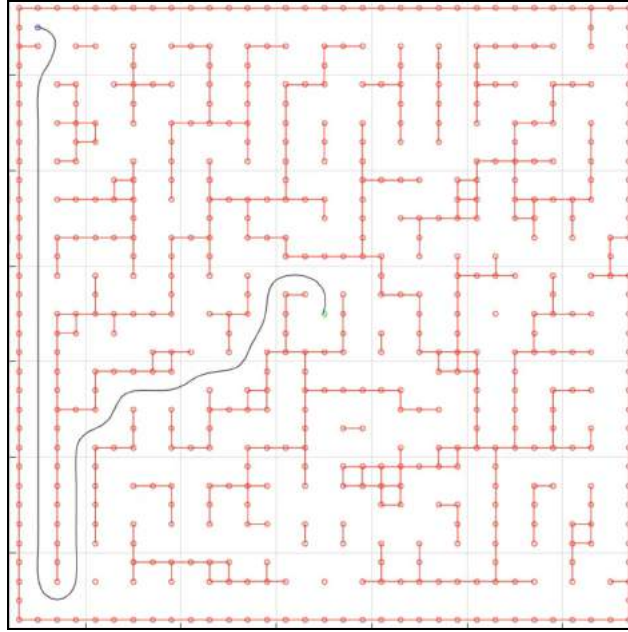


Figure 51. Valid Path Generated Using A* Algorithm and a Known Map (Obstacles in Red).

Robot Test Platform

A robot platform called THOR (Three Omni-Wheeled Platform) was provided by the Drexel University ASME student organization in order to generate datasets using LiDAR and then IMU along with testing autonomy algorithms until the Swerve platform was assembled. **Figure 52** below shows the THOR platform.

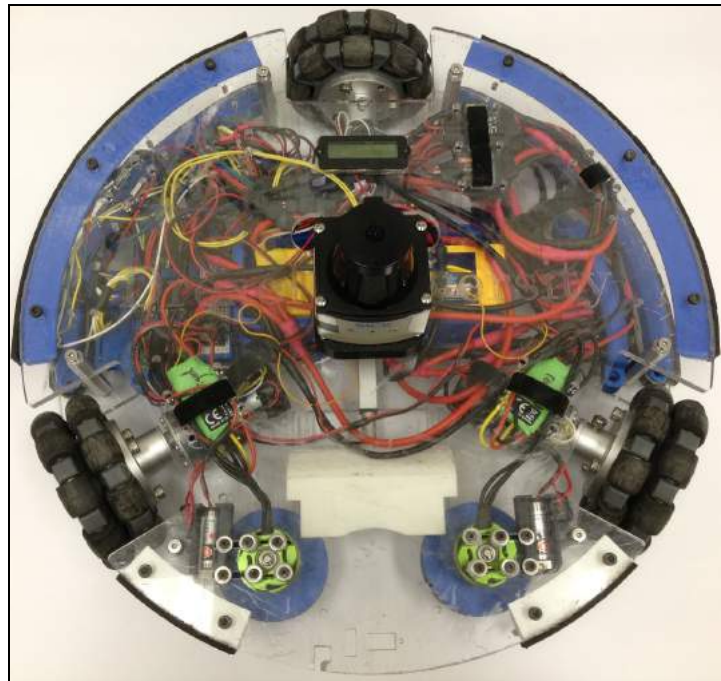


Figure 52. THOR Robot Test Platform with LiDAR Mounted.

The platform comes with an integrated human machine interface through an RC controller along with the a Teensy 3.6 as the central processor. As the name suggests, the platform is omni-directional utilizing omni-wheels which have rotating elements along the outer radius of the wheel to allow the wheel to translate perpendicular to the turning direction passively. THOR mimics the omni-directional kinematic properties of the Swerve platform allowing the platform to be controlled using a similar software architecture as the Swerve platform. The Teensy also has access to the incremental encoders located on each motor that can be used to track the position of the motor over time.

The operator of THOR provides a direction, speed, and spin to the platform through the RC controller. In order to be able to capture LiDAR data and run the Swerve software architecture on THOR, the UpBoard (Swerve onboard computer) was placed on the platform and the BNO055 IMU was connected to the Teensy integrated in the THOR platform. The UpBoard is wifi enabled which allowed for data to be streamed to a remote computer and allow for the platform to be controlled remotely.

This platform was used to test the Swerve software architecture on a physical platform and also generate datasets from the sensors. Data from the sensors were stored in a time-synchronized order and could be played back which allows for the same experiment performed on the THOR platform to be replayed offline in the same time-synchronized order.

Testing and Validation

The stakeholder for the Swerve platform is Joshua Geating, a research and development mechanical engineer at the Naval Research Laboratory who focuses on mechanism design and is interested in robotic platform development. The needs and target expectations for this project specified by our stakeholder are exhibited below in Table 11 .

Table 12. Project Needs and Target Specifications.

#	Needs	Pri.	Metric	Value
1	Highly Nimble	1	Time to Complete Course	< 1 minute
2	Support Heavy Loads	1	Support Static Over-Weight Load	300 lbs
3	Lightweight	1	Weight of Vehicle (Without Power)	100 lbs \pm 10 lbs
4	Human-Machine Interface	1	Remote Control by Human	Yes/No
5	Maintain Ability to be Disassembled	2	No Gross Permanent Connections	Yes/No
6	Faster than Usain Bolt Top Speed	3	Top Vehicle Speed	> 27.8 mph
7	Faster than Usain Bolt Acceleration	3	Top Acceleration	> 19 ft/sec ²
8	Autonomous	3	Navigate Predefined Course	0 Collisions

Welded Material Strength Verification

In order to test the weld strength of the 6061-T6, a four point bend test was conducted. Using an aluminum member similar to the beam components used on the chassis, a sample crush tube was welded in place and used as a test article for the bend test. By evaluating the bending stresses within the member, a nominal stress can be determined to be used as comparison against the published values within the Aluminum Specification. A diagram of the loading configuration and sample equations for the maximum bending stress are shown below.

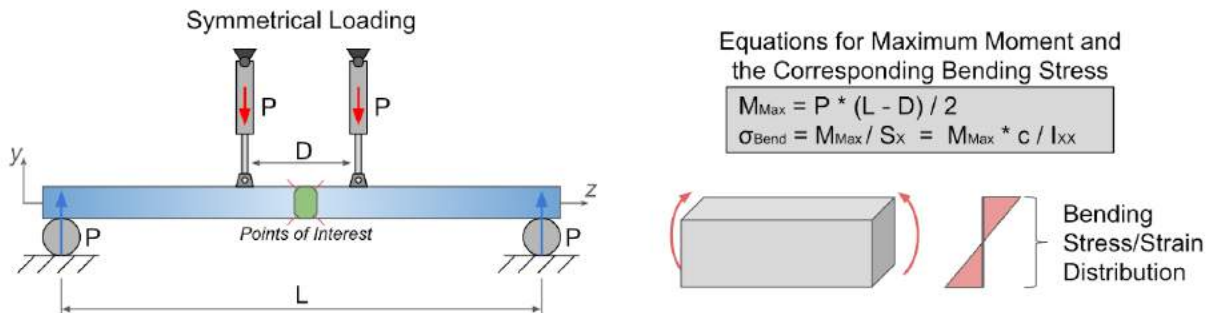


Figure 53. Loading Configuration and Equations for a 4-Point Bend Test.

It was proposed to use stereo digital image correlation (DIC) cameras to characterize the strain field produced by the loading. Additionally a mirror was proposed to allow the camera to view both the tension and compression sides of the loaded test article. Also, acoustic emission (AE) sensors were proposed to determine the time of various damage events. Due to the equipment and software availability, the mirror and acoustic emission sensors were unavailable; however, these missing elements neither hindered nor invalidated the test results. A schematic of the data collection devices is shown below.

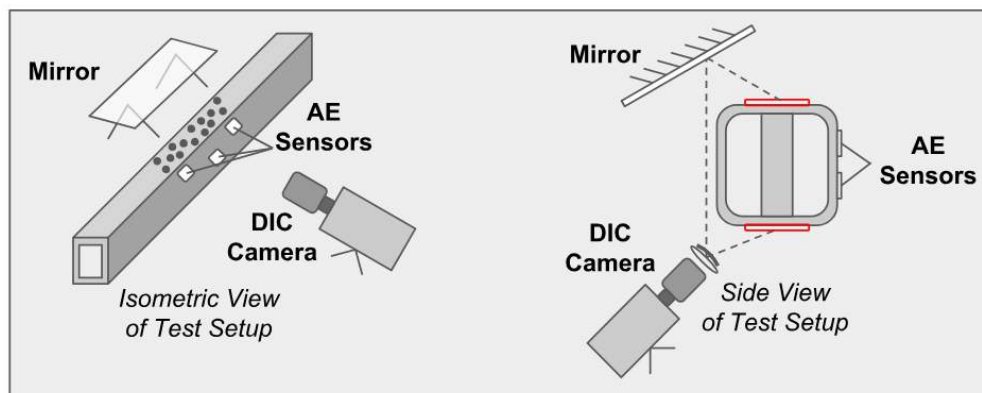


Figure 54. Data Collection Devices for Test - Isometric View (Left) and Side View (Right).

Three aluminum members, each with a sample crush tube welded in place, were loaded in the bend test. The hydraulic actuators applied a monotonically increasing load and the most successful test was load based control for the actuators. This assured that the load between the two actuators was as consistent as possible while the load increased. To remain in the quasi-static regime, the load was applied over the course of about nine minutes, and the load was increased until failure. The stereo DIC cameras were set to record one frame per second. Results from the DIC data are shown below. Both the tension flange and front-facing web of the HSS member are visible in the results. Additionally, the maximum tensile strain, minimum compressive strain, and the actuator applied forces are graphed as well.

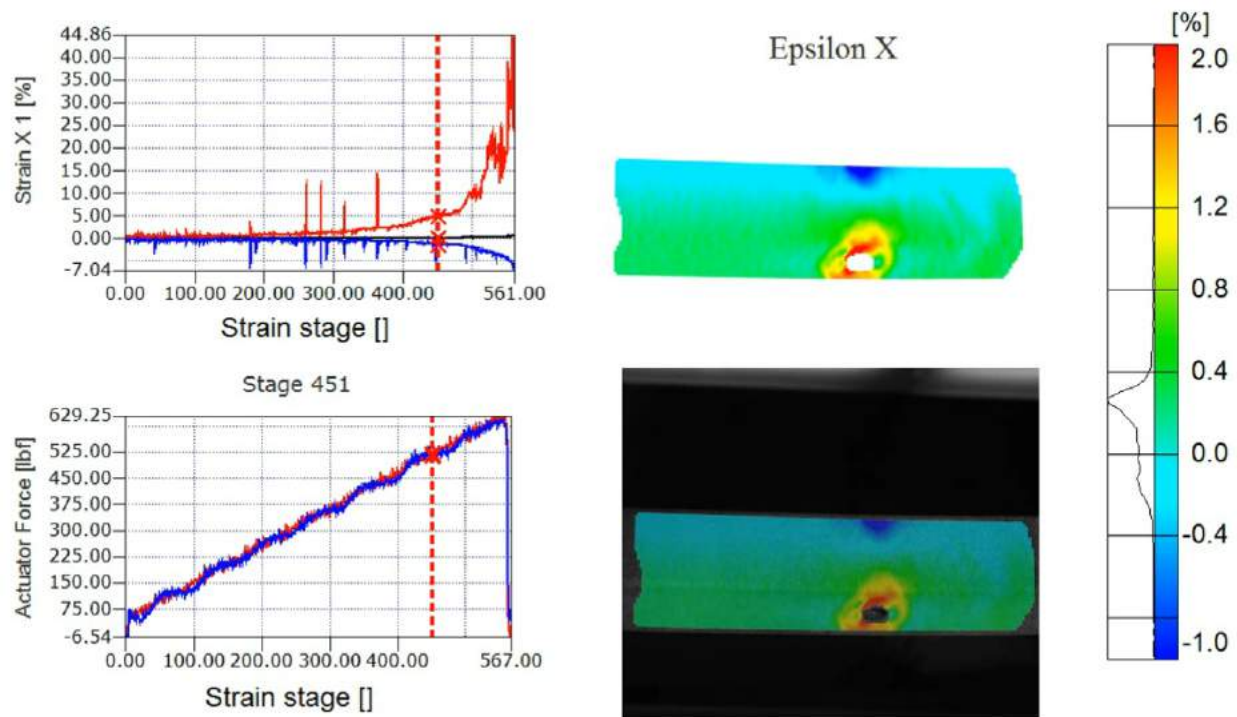


Figure 55. Resulting DIC Data from the Four-Point Bend Test.

It was determined that the crack initiated around strain stage 300 (five minutes elapsed) when the actuator forces were each about 375lbs. This resulted in a nominal bending stress of about 15.5ksi, about 65% of the published weld strength. While the value is well below expected allowables, the finite element analysis conducted was highly conservative, and the simulation stresses reported were evaluated next to singularity points (bolted connections). It is believed that the current design is adequate to support the design loads despite the lowered aluminum welded strength allowable.

Software Architecture Validation

The software architecture was validated using a simulated Swerve platform in the Gazebo physics simulator. The goal of this test was to ensure that the correct communication interfaces and processes were running in order to be able to control the platform and capture data coming from sensors (in this case, simulated sensors). This test involved controlling the simulated platform from a human machine interface on the platform, have the platform move in simulation based on the user inputs, and receiving sensors data back from the simulator. **Figure 56** shows the simulated platform being controlled from the human machine interface and the received the simulated data (LiDAR) in a MATLAB plot on the top right of the figure.

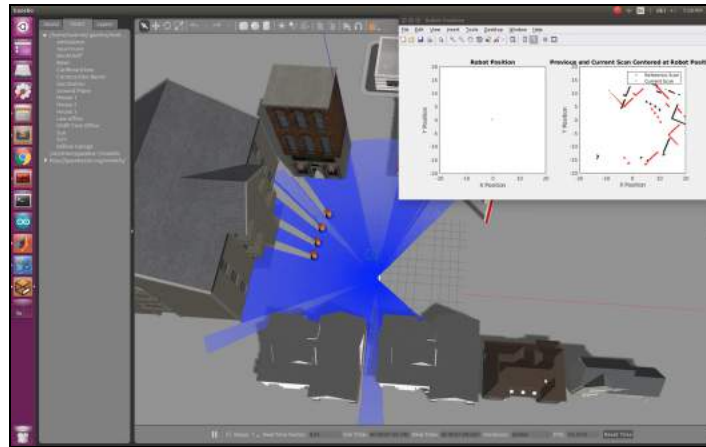


Figure 56. Validating Software Architecture Using Gazebo (LiDAR ray visualized in blue).

Communication Validation

Remote control of the platform was tested in order to ensure the platform would be able to safely operated remotely using the Swerve software architecture. The data from the sensors were also stored in a time-synchronized fashion allowing for the data to be played back to test map generation and localization. The operator remained stationary and controlled the platform using an RC controller. LiDAR data from the platform was streamed through the Drexel University wifi to a remote computer off the platform where the operator was located in order to provide the operator with an understanding of the robot location and its local environment. Using this data, the operator was able to avoid obstacles and pedestrians. One of teams personnel walked with the robot during the test to ensure it did not damage surrounds or injure people.

The test was run for 2401 seconds and the robot travelled 0.55 miles during the duration of the test. During the test, a total of 86.5MB of sensor data was stored in time-synchronized fashion including 36014 LiDAR data messages. It was observed that communication between the remote computer and the THOR platform would drop when switching between routers since the THOR platform was continually moving to new portions of the Drexel University campus. Communication was also dropped more frequently when outside as compared to inside since the onboard computer had less access to nearby routers.

It was determined that with the proper safety features integrated into the Swerve software architecture that the platform was safe to operate remotely. Streaming data through the Drexel University wifi network was unreliable when switching between routers but this issue can be reduced with a more powerful wifi adapter for the onboard computer.

The dataset generated from this test was also used to test the scan matching mapping algorithms. **Figure 48** above shows the results of attempting to generate a map using the LiDAR data from the test. The noise within the dataset causes error in state estimates and does not track rotation robustly causing map to be skewed. With further work, noise within the LiDAR frames can be filtered along with providing the algorithm with better initial state estimate using the other sensors onboard in order to generate cleaner maps.

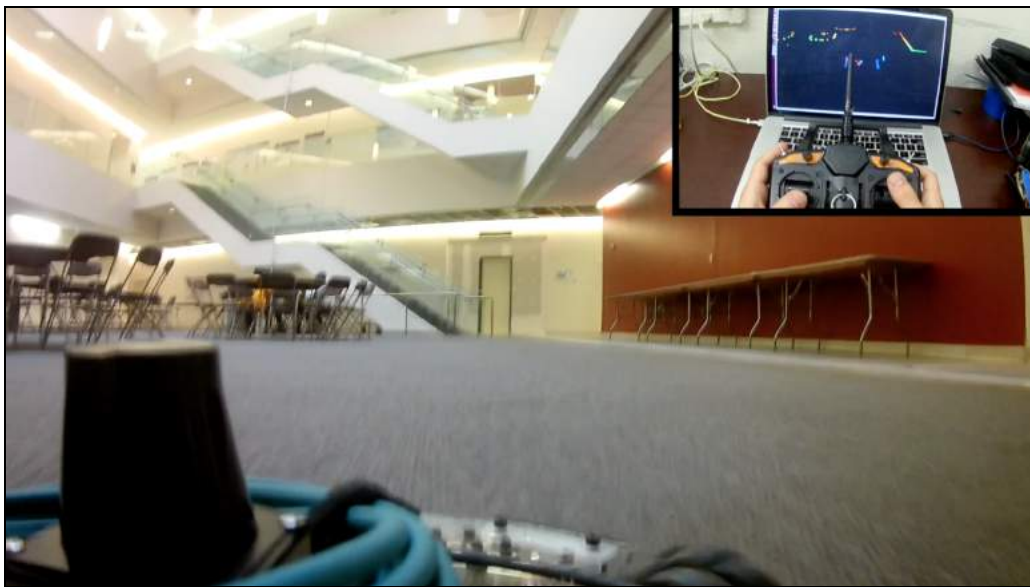


Figure 57. Teleoperating the Robot Test Platform on Drexel University Wifi Network.

Visual Qualitative Validation Tools

A MATLAB GUI was developed in order to visually test and validate the kinematic model. The GUI allows the user to input a desired linear and angular velocity to move the platform along with allowing the user to click a location on the GUI that the robot should rotate around. Since the kinematics is defined around the circle radius pseudo state, as described in the *Kinematic and Dynamic Modeling* section above, the location of the user click and the current location of the simulated robot at the time of the screen click determines the radius parameter.

As seen below in **Figure 58**, the vehicle visually appears to operate correctly.

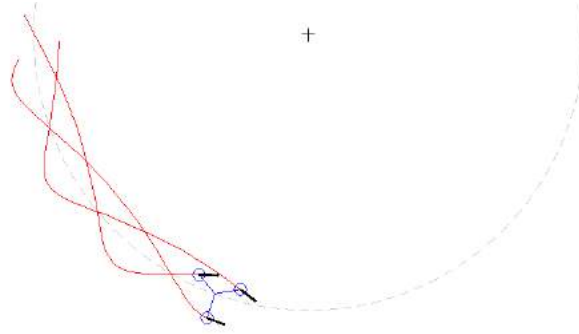


Figure 58. MATLAB GUI to Visually Validate Platform Kinematics.

Autonomy Algorithm Validation and Dataset Generation

In order to be able to test the platform autonomy algorithms correctly and be able to validate the accuracy of estimating the state of the robot over time, ground truth data of the platform location is needed for comparison. The test platform, THOR, was brought into a motion capture room that had 16 highly accurate VICON cameras around the perimeter of the room tracks markers placed on the THOR in order to triangulate the position of THOR in the room down to a sub-millimeter accuracy.

A dataset of running THOR is one of these motion capture rooms with consistent obstacles was generated storing both the sensor data from THOR and the ground truth data of THOR and the obstacles from the VICON motion capture system. **Figure 59** below shows THOR in the motion capture room with the upper right window showing the viewpoint of the robot from a camera placed on THOR and the top left window shows a live visualization of the platform position and LiDAR data. This test was performed three times in order to generate different datasets to test the autonomy algorithms on. An additional test was performed with the platform static in order to generate a model of the static error on the onboard sensors for calibration and noise reduction.

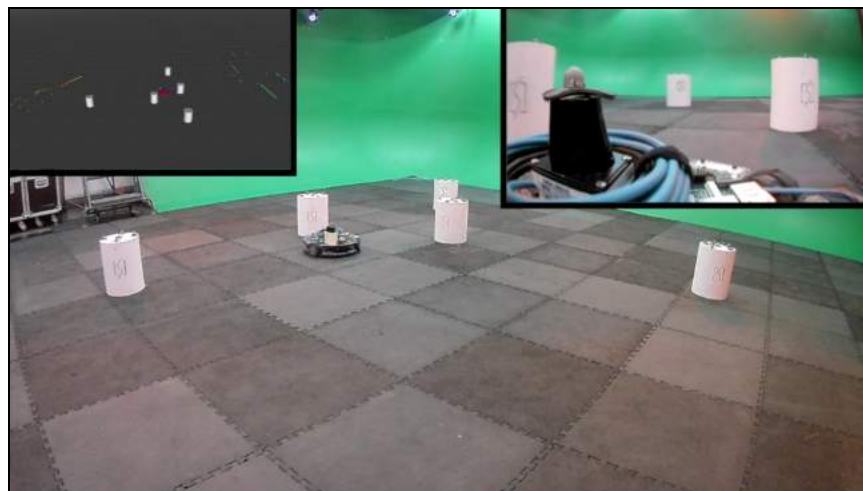


Figure 59. Teleoperating the Robot Test Platform in a Motion Capture Room with Obstacles.

Below is a table outlining four datasets that were generated from these tests. **Figure 60** shows an attempt at generating occupancy grids using filtered LiDAR data from *Dynamic Dataset 3*.

Table 13. VICON Motion Capture Dataset Information.

Data Set Title	File Size	LiDAR Messages	IMU Messages	Encoder Messages
Dynamic Data Set 1	52.3 Mb	1,989	926	924
Dynamic Data Set 2	90.1 Mb	2,413	1,608	1,605
Dynamic Data Set 3	88.4 Mb	1,755	1,172	1,172
Static Data Set 1	35.5 Mb	923	616	616

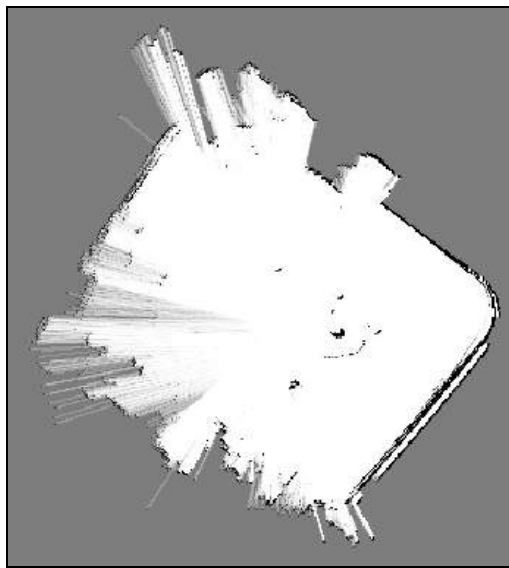


Figure 60. Occupancy Grid Generated from Dynamic Dataset 3.

Vehicle Weight Validation

The team utilized a standard bathroom scale in order to validate the overall weight of the vehicle one person will stand on the scale and record their weight. The person then stood on the scale while holding the vehicle. The difference between the two weights was the calculated vehicle weight of 55 lbs. The stakeholder has deemed the accuracy of a bathroom scale sufficient. The range of measurement of a bathroom scale is well within the estimated weight of a team member holding the vehicle. The result of the validation is a mechanical vehicle weight of 55lbs, the electronics and battery are estimated to be ~10 lbs, which complies with the specified target specification.

Future Work

Finite Element Model Validation

In order to validate the finite element model, a known load case will be simulated in the software and replicated with the fully fabricated vehicle. For convenience, the 300lbs dead load (only gravitational acceleration) will be applied in the model. Then, using the fabricated vehicle, digital image correlation will be used to determine the strain field on the existing components. Once the strain value is determined, it will be compared to the simulation strain field in the same location. This will determine how accurate the finite element model was, and depending on the outcome, the other finite element simulations may be scaled according to the percent error. Below is a stress contour plot of the simulated 300lbs dead load case with selected locations to analyze on the existing platform. The finite element model will be considered accurate if the strains on the fabricated vehicle are within 10% of the predicted simulation values.

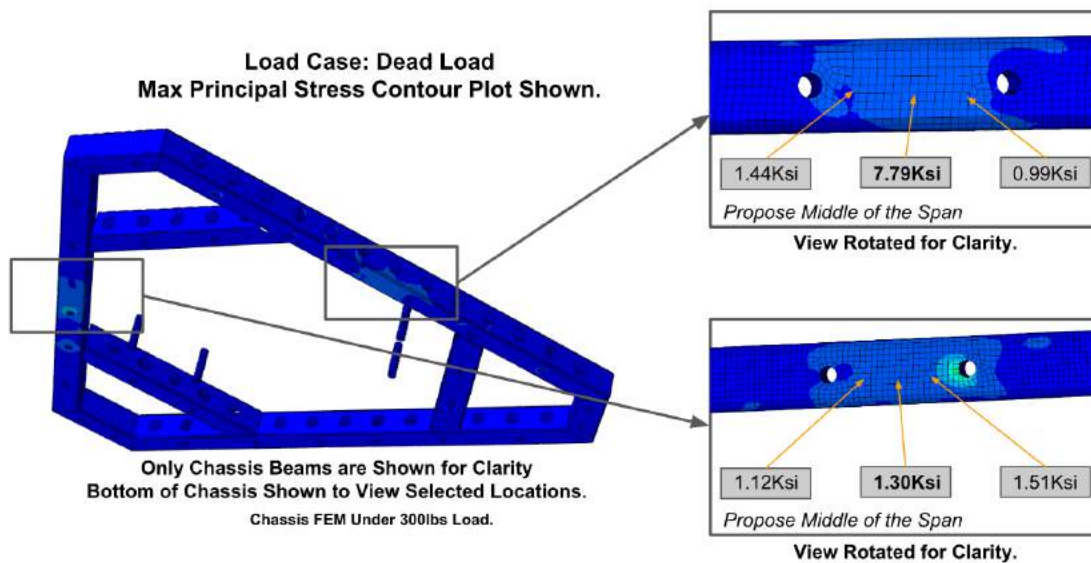


Figure 61. Max Principal Stress Contour Plot of Chassis Under 300lbs
Locations Shown Include Areas for Strain Measurements.

Speed and Acceleration Testing

As a reach goal with low priority, the team will test the top speed and maximum acceleration of the Swerve vehicle and compare the results to Olympian Usain Bolt. Thanks to researchers at the University of California Davis [13], a detailed measurement of Usain Bolt's distance vs. time has been recorded, plotted, fitted with a regression model, and integrated in order to find his velocity vs. time and acceleration vs. time curves over the course of his famous 2008 100 meter dash. The results can be seen below in **Figure 62**.

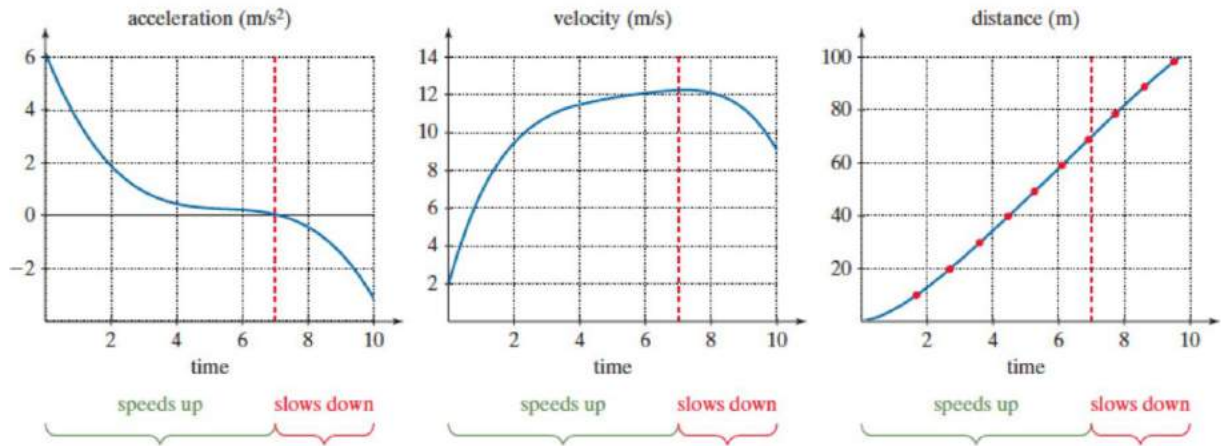


Figure 62. Position, Velocity, and Acceleration Curves of Usain Bolt Across 100 Meters.

The test setup to record our own distance vs. time plot across 100 meters consists of a 100 meter stretch of flat land, potentially at Drexel's Recreational Center. The vehicle will perform the 100 meter dash while being recorded from multiple angles. The video recordings will be recorded and position vs. time data will be extracted and converted into velocity and acceleration curves that can be compared to the ones above in **Figure 62**.

Agility Testing

The designated test course consists of 10 cones arranged in the pattern depicted below in Figure 63. The robot will start in a forward orientation, “swerve” through a set of 6 cones placed 6 feet apart while maintaining the forward direction, at the end of the 6 cones the vehicle will change its direction to face sideways and perform the course in reverse while maintaining the new orientation. This course is designed to replicate the motions that a dextrous human can achieve but traditional nonholonomic mobility systems can not achieve as gracefully.

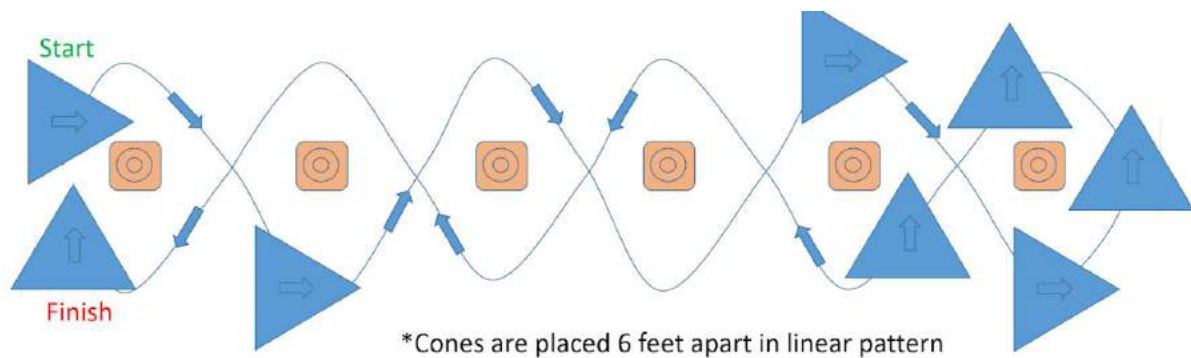


Figure 63. Designated Course Setup to Verify Needs 1 and 2.

Closing Remarks

The Swerve Robotic Platform is designed and engineered to be a three-wheeled, omnidirectional, autonomy-enabled mobile platform. The vehicle is intended to be as lightweight and as nimble as possible by incorporating holonomic movements and high-torque, high-velocity brushless DC motors. Each of the three wheels is capable of independent yaw and propulsion. Additionally the vehicle is designed and analyzed to carry payloads up to 300lbs without appreciable damage, and it is capable of traveling at speeds exceeding 28 miles per hour and accelerations up to 32.2 ft/s^2 (1G).

Throughout the course of this project, the Swerve team has identified a need, created target specifications, and proceeded through multiple design iterations. These designs were optimized for a light-weight yet high performance vehicle, in which design was influenced by Finite Element Analysis as well as multiple industry standards. A critical design review was performed and feedback was received from academia as well as industry advisors. Advanced manufacturing techniques were used in order to meet the aggressive project timeline. Autonomous LiDAR sensing was implemented and tested; and controllability ground truth data has been collected using a ViCON motion capture studio. The vehicle as well as bulk material was tested using Digital Image Correlation at Drexel University's TAMG Lab. Finally, full vehicle testing is currently on going and the project is on track to successfully deliver the platform to the stakeholder.

The interdisciplinary team has allowed each member to bring a specialized background to the project: mechanical analysis, manufacturing, controls, and autonomy. The collaborative work between the Swerve Team, Drexel's Animations Department, NextFAB Makerspace, Drexel's Machine Shop, and Drexel University's TAMG Laboratory has strengthened the project, the perspective of the team members, as well as Drexel University.

Links to Detailed Design Review Documents

swerveroboticsystems.github.io/DDR/Design

swerveroboticsystems.github.io/DDR/Analysis

swerveroboticsystems.github.io/DDR/Software

References

- [1] ASTM International F2291-17 “*Standard Practice for Design of Amusement Rides and Devices*” 2017.
- [2] American Institute of Steel Construction 360-16 “*Specification for Structural Steel Buildings*” 2016.
- [3] FRC Team 1717. “2012 FRC Team 1717 Uncut: Swerve Drive”, [online] Available at: <https://www.youtube.com/watch?v=kZHaTGiaKZM> [Accessed 30 Nov. 2017].
- [4] NASA. “When NASA develops a swerve drive car”, [online] Available at: <https://www.youtube.com/watch?v=eE0KwnDYYh8> [Accessed 30 Nov. 2017].
- [5] Fetch Robotics. “Fetch Automates Your Warehouse With Robots”, [online] Available at: <https://www.youtube.com/watch?v=CEIUrf7iOXk> [Accessed 30 Nov. 2017].
- [6] D.O.T, “*Metallic Materials Properties Development and Standardization*”. January, 2003.
- [7] J. Randolph Kissell. “*Aluminum Structures: A Guide to Their Specifications and Design*” 2002.
- [8] John Wiley and Sons. “*The Measures of Man and Woman Revised Edition*”. Human Factors in Design. 2002.
- [9] Research Council on Structural Connections “*Specification for Structural Joints Using High-Strength Bolts*” 2014.
- [10] Biber, P., and Strasser, W. “The Normal Distributions Transform: A New Approach to Laser Scan Matching.” Intelligent Robots and Systems Proceedings. 2003.
- [11] Milstein, A. “Occupancy Grid Maps for Localization and Mapping.”, Motion Planning, Xing-Jian Jing (Ed.), 2008. ISBN: 978-953-7619-01-5, InTech, Available from: http://www.intechopen.com/books/motion_planning/occupancy_grid_maps_for_localization_and_mapping
- [12] Doucet, A., Johansen, A. “A Tutorial on Particle Filtering and Smoothing: Fifteen years later.” 2012.
- [13] S. Schreiber, W. Getz, K. Smith. “Calculating just how fast Usain Bolt runs” Egghead:About Research at UCDavis, Blog Article 2016.
- [14] Walter D. Pilkey, “*Peterson’s Stress Concentration Factors, Third Edition*” 2008.

Acknowledgements

The Drexel University Swerve Robotic Platform 2018 senior design team would like to thank the following people for their support and advising.

Project Stakeholder

We would like to thank Joshua Geating for his financial support of the project, advising, and working with the team to ensure we produce a successful product.

Project Advisors

We would like to thank Dr. Ajmal Yousuff for his willingness to be our head advisor, providing us support on dynamic modeling, and advising throughout the course of the project. We would also like to thank our co-advisor Dr. Tein-Min Tan for his support with finite element modeling and mechanical analysis along with advising throughout the course of the project.

Project Sponsors

We would like to thank George Thiel from SICK Sensors, Chuck Sacco and the Botstiber Senior Design Competition Committee, the ASME Philadelphia Section, and the Drexel University Mechanical Engineering Department for their financial support of our senior design project.

Drexel University Animation, Capture & Effects Lab (ACE-Lab)

We would like to thank Nick Jushchyshyn for allowing us to use his VICON motion capture facility and providing support on streaming data to our robot test platform.

Drexel University Theoretical and Applied Mechanics Laboratory (TAMG)

We would like to thank Dr. Antonios Koutsos, Dr. Brian Wisner, and Melvin Mathew for allowing us to use of their facility and providing support with performing DIC camera testing with a four point bend test along with static load testing of our platform.

Drexel University Machine Shop

We would like to thank Mark Shiber, Scott Eichmann, and Nick Catucci at the Drexel Machine Shop for their aid in manufacturing, welding, and 3D CNC milling.

External Reviewers and Advising

We would like to thank Eric Vance for his support on mechanical design review and technical guidance during the detailed design review phase, Dr. Li-Hsin Han for support on developing the dynamic model for the platform, and Dani Liu for her support in the initial development of the finite element model in ABAQUS.

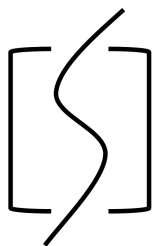
Drexel University College of Engineering (COE) Information Technology (IT) Department

We would like to thank the Drexel COE IT department for their assistance in setting up our hardware to work properly with the Drexel University network.

NextFab

We would like to thank NextFab for their support in providing design and machinability advice as well as access to their advanced manufacturing equipment.

This page is intentionally left blank



Appendix

Design and Analysis Process

Mechanical Design Process

The governing design criteria for the chassis were size and weight, with the goal to minimize both. With a high strength to weight ratio, as well as a high material availability, it was determined that 6061-T6 should be used to fabricate the structural components of the chassis. Additionally, it was preferred that the chassis was not a permanent structure and easily disassemblable for transportation and modularity. To satisfy those criteria, it was determined that the chassis would be constructed with structural bolted connections as opposed to welding or adhesives. Throughout the design process, multiple iterations of the chassis were developed and modified to find a design that satisfied and optimized all criteria.

To take advantage of the strength to weight ratio, hollow structural sections (HSS) of 6061-T6 were chosen as the main structural components for the chassis. The HSS beams are connected using gusset plates that span multiple beams. However, since it was determined that the structure needed to be bolted together, crush tubes are welded into place in order to prevent the HSS from warping or buckling under bolt preload. These crush tubes are manufactured from 6061-T6, and they are groove welded and ground flush into place. In order to provide a flush surface for the payload, countersunk bolts are used to connect all components on the chassis.

The mechanical design of this swerve assembly has undergone a multitude of iterations over the course of Summer and Fall 2017. Three major design iterations can be seen below. Significant aspects that affected these design decisions were wheel size and type, bearings selection, bearing position, wheel housing structural design, motor mounting systems, and belt tensioning systems. A few highlights of these considerations include moving from a linear slotted hole motor mount on the left and center images below to the rotation motor mount system on the right in the image below. This rotating motor mount allows the motor to be fastened permanently while adjusting the tension separately, which is advantageous for fine tuning of the belt tension.

Another highlight of the design iteration process is the choice of wheel size. On the center and left images below, an eight inch diameter pneumatic wheel was chosen since it could easily interface with a consumer off the shelf (COTS) pulley. For the final iteration, a smaller five inch diameter pneumatic wheel was chosen since it increases the potential acceleration for the vehicle, but requires a COTS pulley to be modified in order to fit the wheel. These kinds of design trades were common across the entire vehicle from the bearing choice to the wall thickness of the chassis tubing. Ultimately, the picture on the right in the figure below is a matured design ready for design review by stakeholders, advisors, and industry professionals.

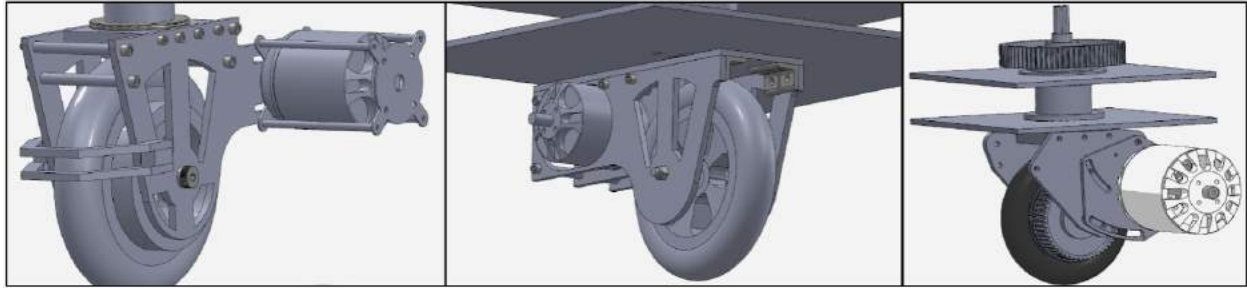


Figure A1. Mechanical iterations of swerve drive assembly.

Structural and Mechanical Analysis Process

Since the platform is a prototype that is intended for personal use, fatigue and environmental factors were ignored, per the stakeholder's request. Initial hand calculations were conducted to determine the largest allowable size of the platform while still passing the required strength safety factors.

To address the inherent indeterminacy in the structure, finite element modeling was chosen for the structural analysis. ANSYS Workbench was initially used to create the finite element (FE) model, though due to node limits and license constraints, it was determined that the software package would not allow the resolution required to analyze the local effects on the structure. Instead, ABAQUS/CAE was used to create the finite element models since the node limits were higher than ANSYS Workbench.

The solid models created in SolidWorks were exported to ABAQUS for analysis. Although parasolids are preferred to transfer the geometry, IGES files were exported instead since there were additional licensing issues with ABAQUS/CAE. Within SolidWorks, the non-structural components of the chassis assembly were removed, and then the remaining components were exported to be analyzed in ABAQUS. Additionally, the non-structural components were removed from the wheel assembly, and the remaining components were also exported to be analyzed in ABAQUS. Within the ABAQUS/CAE interface, the plate and tube components on the chassis and wheel assembly instances were midsurfaced and preprocessed for analysis. The wheel assembly includes small holes for mounting electronics and sensors. These holes affect the mesh size and can increase the solve time. The model is idealized by removing these small holes and a nominal stress through the section is determined by the finite element solver. Using the stress concentration equations below, the adjusted stress can be calculated. For simplicity, the same concentration factor equations apply to holes in near proximity to others.

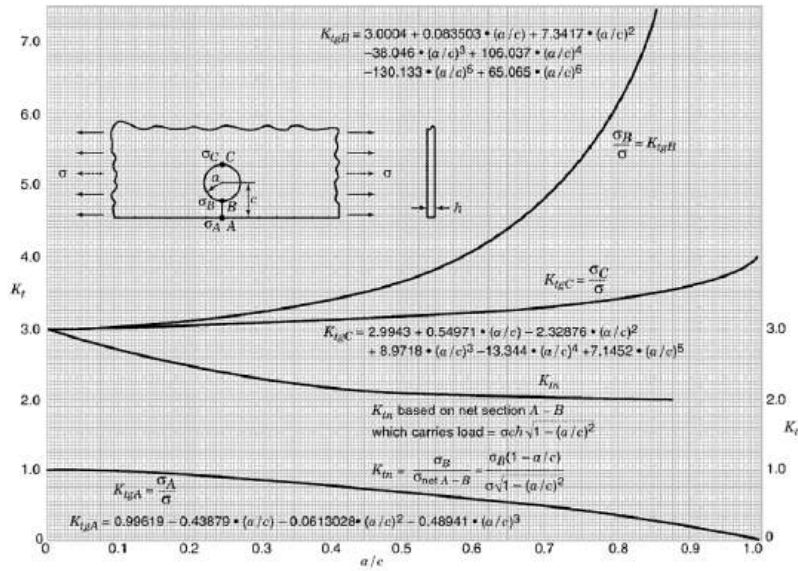


Chart 4.2 Stress concentration factors for the tension of a thin semi-infinite element with a circular hole near the edge (Uduguti 1947; Mindlin 1948; Isida 1955a).

Figure A2. Stress Concentration Factors for Tension Plates with Holes Near Edges [14].

To accurately analyze the bolted connections, preload values for the structural connections were required. Using Table 7.1 presented in the *Specification for Structural Joints Using High-Strength Bolts* from the Research Council on Structural Connections (RCSC), a quadratic fit was calculated using the documented values, and different bolt pretensions were determined. The quadratic fit and interpolated preload values are shown below.

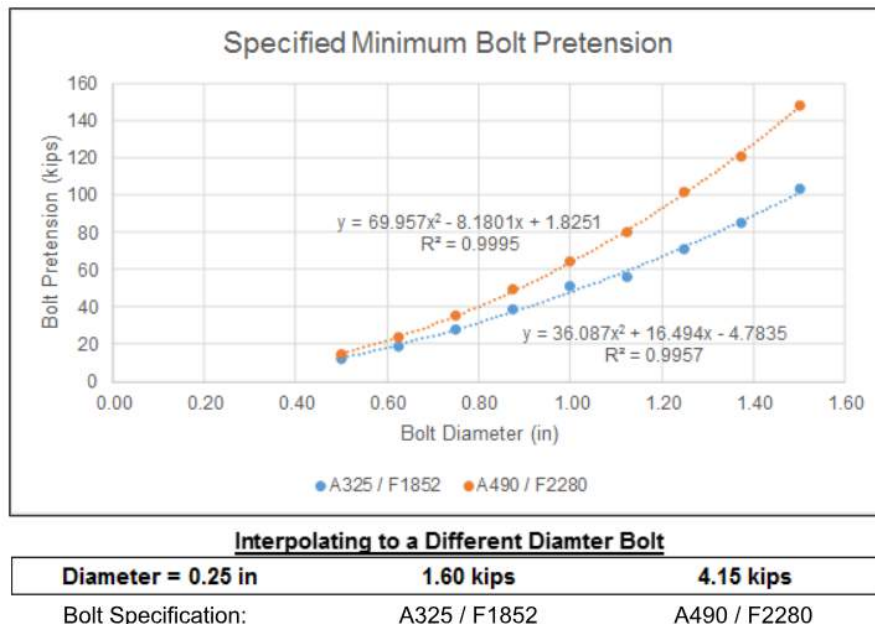


Figure A3. Quadratic Fit Given AISC Bolt Preload Values and Interpolated Preloads.

Initially, the connection between the gusset plates and the chassis beams included an 82deg flathead bolt inserted in a countersink within the gusset plates. Due to the small thickness of the gusset plates, the reduction in area from the countersink resulted in a cross-sectional area that was too small to react the bearing loads transferred by the shank of the bolt. Instead, it was determined that 100deg flathead would be required since the higher angle results in a larger shank area. The force diagrams and accompanying calculations are shown below.

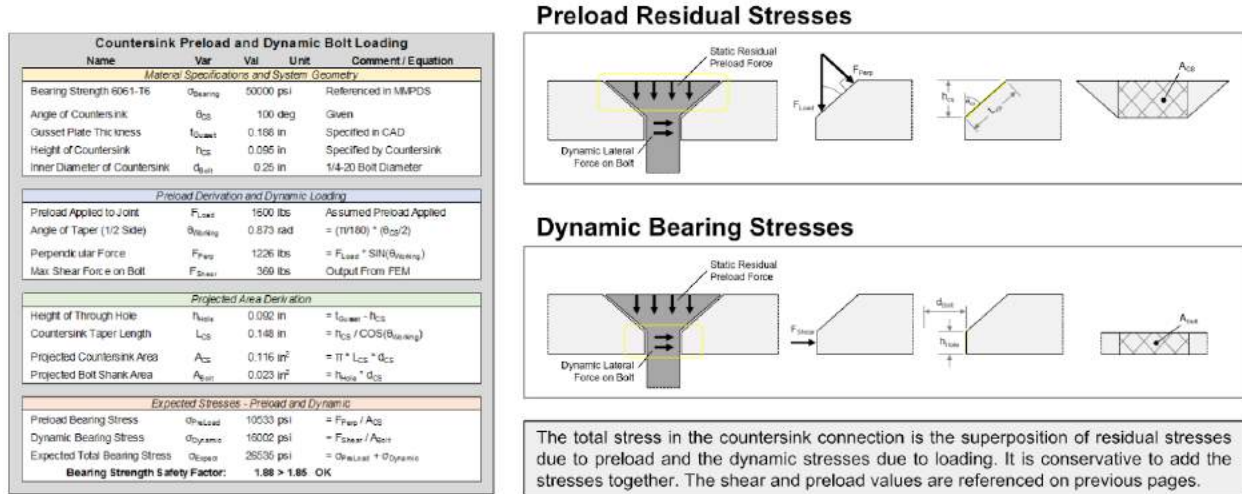


Figure A4. Countersink Bolt Force Diagrams and Resulting Calculations.

Protocol Comparison for Communicating with VESC's

The CAN protocol is often preferred for real time communication, as is the case on the platform. It can easily allow for more CAN devices to access the network and has a better fault handling system. CAN is more difficult to implement without the availability of an already existent CAN library. The UART protocol is easy to implement but is meant for communication between only two devices and is not good for fault handling when compared to CAN.

Further Optimization with Path Planning

As mentioned in the *Algorithms and Autonomy* section of the *Final Design Package*, A* and RRT can be used to generate valid paths for the robot to follow. More efficient paths can be generated using more complex algorithms like finite horizon and receding horizon model predictive controller. These controllers allow for the incorporation of the platform dynamic model in order to generate paths that are valid to the mechanical properties of the system along with providing the controller with path constraints, for example time or energy usage, in order to guarantee the generated path is optimal to the heuristic. Combining model predictive control with particle filters, occupancy grids, and obstacle avoidance can allow the platform to operate fully autonomously if desired.

Electronics Safety Features Additional Information

The platform comes with a single mechanical switch that only powers off the main electronics (everything other than the motor controllers) as described in the *Electronics* section of the *Final Design Package*. If desired, an additional mechanical switch can be incorporated in order to shut off power to all devices on the platform. This component would be expensive since it would need to handle up to 850A (600A from three drive motors, 240A from yaw motors, 10A from electronics) which is why this switch is not incorporated onto the platform.

Project Management

Personnel

The team consists of four members. Harrison Katz and Matthew Wiese form the mechanical focus team who are responsible for the mechanical design, mechanical analysis, and fabrication. Alexander Nhan and Frederick Wachter form the software focus team who are responsible for building the platform software architecture along with interfacing with all the electrical hardware. The team is advised by Dr. Ajmal Yousuff (Head Advisor), Dr. Tein-Min Tan (Co-Advisor) and Joshua Geating (Stakeholder).



Figure A5. Images of Team Personnel.

Organizational Tools

The team used Slack for communication, Google Drive for file sharing, and Github for remote software hosting. The team met weekly in order to go over critical elements of the project and give tasks to each of the members. The team met bi-weekly with advisors and stakeholders to go over project progress and any issues.

Software Usage

The team used SolidWorks for CAD, ANSYS and ABAQUS for FEM, Fusion 360 for CAM, MATLAB for dynamics, kinematics, and algorithm development, ROS for the software framework and hardware interfaces, Doxygen for auto-generating software documentation, Git for software version control, and Gazebo for simulated platform testing.

Project Schedule

Figure # below outlines the final project schedule.

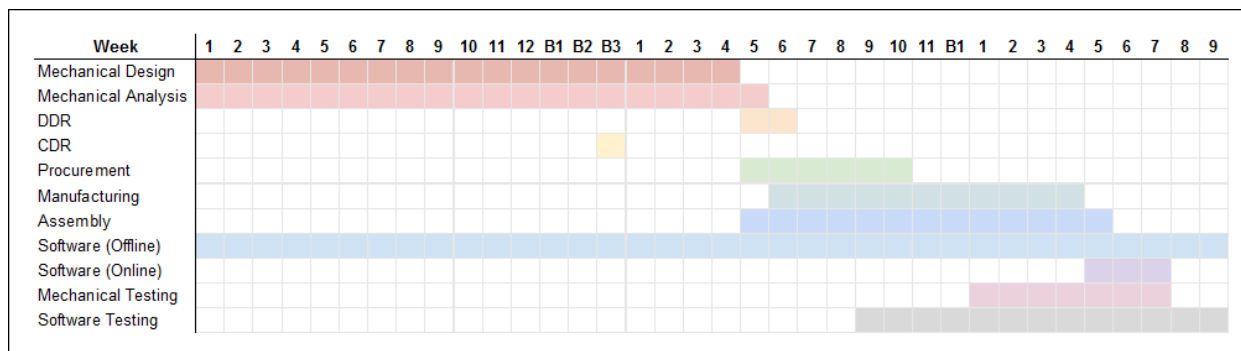


Figure A6. Finalized Project Schedule.

Review Processes

The team went through a set of three review processes in order to ensure the platform met the expectation of the stakeholder than that the engineering assumptions made were correct. **Table 13** below outlines the review processes that were performed.

Table A1. List of Review Processes.

SRR - *System Requirements Review* - July, 2017

DDR - *Detailed Design Review* - December, 2017

CDR - *Critical Design Review* - December, 2017

PHO - *Prototype Hand-Off to Stakeholder* - June, 2018

Project Budget

The Swerve platform costs \$3,100.62 for the mechanical hardware and \$4,756.89 for all the sensors and electronics. The total project cost was \$7,857.51. The team received a total of \$7,857.51 in funding as shown in **Table 14**.

Table A2. High Level Project Costs.

Part Number	Description	Unit Cost	Qty	Ship	Total
Mechanical Hardware					
23438	2.0in. X 0.12in. SQ. and 0.25in Rad 6061-T6	\$ 38.33	3	\$ -	\$ 114.99
1247	24.0in. X 48.0in. X 0.19in. Sheet, 6061-T6	\$ 127.04	2	\$ -	\$ 254.08
9544	0.625in. OD X 0.125in Tube, 6061-T6	\$ 60.01	2	\$ -	\$ 120.02
15021	2.5in. Dia Bar, 8620 Hot Rolled Steel	\$ 95.13	1	\$ -	\$ 95.13
24233	1/4-20 X 3in. Flat Socket Cap Screw	\$ 0.68	114	\$ -	\$ 77.47
169776	1/4-20 Nylon Insert Lock Nut, Grade 5	\$ 0.29	200	\$ -	\$ 58.38
33813	1/4" X 0.625" Hardened Washer, Yellow Zinc	\$ 11.16	1	\$ -	\$ 11.16
33078	1/4" X 0.625" General Washer, Zinc	\$ 0.04	200	\$ -	\$ 8.04
95011	1/4-20 X 2in. Hex Cap Screw, Yellow Zinc	\$ 0.33	50	\$ -	\$ 16.33
95005	1/4-20 X 1in. Hex Cap Screw, Yellow Zinc	\$ 0.21	50	\$ -	\$ 10.44
61911-2RS1	55mm ID, 80mm OD, Ball Bearing	\$ 280.13	6	\$ 9.98	\$ 1,690.76
51111	55mm ID, 78mm OD, Thrust Bearing	\$ 85.91	6	\$ 9.98	\$ 525.44
A 6A55M028DF0912	5mm Pitch, 12mm Bore, 28 Teeth, Timing Pulley	\$ 16.04	6	\$ -	\$ 96.24
A 6Z25M015DF0908	5mm Pitch, 8mm Bore, 15 Teeth, Timing Pulley	\$ 7.38	3	\$ -	\$ 22.14
Grand Total Mechanical Hardware:					\$ 3,100.62
Sensors and Electronics					
900-83310-0001-000	NVidia Jetson TX2	\$ 299.00	1	\$ -	\$ 299.00
DEV-14057	Teensy 3.6	\$ 29.25	4	\$ -	\$ 117.00
Tim561-2050101	High-Accuracy LIDAR	\$ 2,599.00	1	\$ -	\$ 2,599.00
387000075-0	Ublox NEO-M8N GPS Module	\$ 19.99	1	\$ -	\$ 19.99
-	ZED Camera	\$ 449.00	1	\$ -	\$ 449.00
-	VESC Motor Controller	\$ 99.00	6	\$ -	\$ 594.00
WRL-09411	Xbee Xtend 900MHz	\$ 194.95	2	\$ -	\$ 389.90
RE-UPS-APLP4-A10-0864	UpBoard Squared	\$ 289.00	1	\$ -	\$ 289.00
Grand Total Sensors and Electronics:					\$ 4,756.89

Table A3. Total Project Funding.

Monetary Support

Josh Geating: \$3,158.51

Drexel MEM Department: \$ 500.00

ASME Philadelphia: \$ 600.00

Botstiber Senior Design Project: \$1,000.00

Hardware Samples

SICK Sensors: \$2,599.00